Statistical Properties of Superflares on Solar-type Stars: Results Using All of the Kepler Primary Mission Data

Soshi Okamoto[1], Yuta Notsu[2,3,8] , Hiroyuki Maehara[4,5] , Kosuke Namekata[1,9] , Satoshi Honda[6], Kai Ikuta[1] ,
Daisaku Nogami[1], and Kazunari Shibata[7]

[1] Department of Astronomy, Kyoto University, Sakyo, Kyoto 606-8502, Japan; sokamoto@kusastro.kyoto-u.ac.jp
[2] Laboratory for Atmospheric and Space Physics, University of Colorado Boulder, 3665 Discovery Drive, Boulder, CO 80303, USA
[3] National Solar Observatory, 3665 Discovery Drive, Boulder, CO 80303, USA
[4] Okayama Branch Office, Subaru Telescope, National Astronomical Observatory of Japan, NINS, Kamogata, Asakuchi, Okayama 719-0232, Japan
[5] Okayama Observatory, Kyoto University, Kamogata, Asakuchi, Okayama 719-0232, Japan
[6] Nishi-Harima Astronomical Observatory, Center for Astronomy, University of Hyogo, Sayo, Hyogo 679-5313, Japan
[7] Kwasan Observatory, Yamashina, Kyoto 607-8471, Japan

Abstract

We report the latest statistical analyses of superflares on solar-type (G-type main-sequence; effective temperature is 5100–6000 K) stars using all of the Kepler primary mission data and Gaia Data Release 2 catalog. We updated the flare detection method from our previous studies by using a high-pass filter to remove rotational variations caused by starspots. We also examined the sample biases on the frequency of superflares, taking into account gyrochronology and flare detection completeness. The sample sizes of solar-type and Sun-like stars (effective temperature is 5600–6000 K and rotation period is over 20 days in solar-type stars) are $\sim$4 and $\sim$12 times, respectively, compared with Notsu et al. As a result, we found 2341 superflares on 265 solar-type stars and 26 superflares on 15 Sun-like stars; the former increased from 527 to 2341 and the latter from three to 26 events compared with our previous study. This enabled us to have a more well-established view on the statistical properties of superflares. The observed upper limit of the flare energy decreases as the rotation period increases in solar-type stars. The frequency of superflares decreases as the stellar rotation period increases. The maximum energy we found on Sun-like stars is 4×10^{34} erg. Our analysis of Sun-like stars suggests that the Sun can cause superflares with energies of $\sim 7 \times 10^{33}$ erg ($\sim$X700-class flares) and $\sim 1 \times 10^{34}$ erg ($\sim$X1000-class flares) once every $\sim$3000 and $\sim$6000 yr, respectively.

Unified Astronomy Thesaurus concepts: Flare stars (540); Optical flares (1166); Stellar flares (1603); G dwarf stars (556); G stars (558)

Supporting material: machine-readable table

1. Introduction

Flares are explosions in the stellar atmosphere with an intense release of magnetic energy stored around starspots (e.g., Shibata & Magara 2011). The typical total bolometric energy of solar flares ranges from 10^{29} to 10^{32} erg (e.g., Crosby et al. 1993; Aschwanden et al. 2000; Shibata & Yokoyama 2002), and the duration ranges from a few minutes to a few hours (e.g., Veronig et al. 2002; Namekata et al. 2017). Many other stars besides the Sun also show magnetic activities such as flares. In particular, young rapidly rotating stars, close binary stars, and dMe stars show much higher levels of magnetic activity than the Sun (e.g., Gershberg 2005; Reid & Hawley 2005; Benz & Güdel 2010; Kowalski et al. 2010; Osten et al. 2016; Linsky 2019; Namekata et al. 2020b). They often causes "superflares," which have total bolometric energies 10^1–10^6 times more energetic than the largest solar flares ($\sim 10^{32}$ erg; Emslie et al. 2012). On the other hand, since the Sun is old and rotates slowly (rotation period $P_{\rm rot} \sim 25$ days), it had been thought that the Sun and slowly rotating Sun-like stars ($P_{\rm rot} > 20$ days) would not show superflares. However, many solar-type (G-type main-sequence, MS) stars, including slowly rotating Sun-like stars, showed that superflares have recently been reported by using the Kepler space telescope (Maehara et al. 2012, 2015; Shibayama et al. 2013; Candelaresi et al. 2014; Wu et al. 2015;

Balona 2015; Davenport 2016; Van Doorsselaere et al. 2017; Notsu et al. 2019) and TESS (Tu et al. 2020; Doyle et al. 2020).[10]

Since solar flares sometimes lead to magnetic storms on the Earth, serious damage may be caused in our modern lives if a superflare occurs on the Sun (e.g., Baker 2004; Takahashi et al. 2016; Riley et al. 2018; Battersby 2019). Electrical currents induced by geomagnetic storms can cause significant damage to ground electrical transmission equipment, leading to a widespread blackout. For example, on 1989 March 13, in Quebec, Canada, about 6 million people suffered an electrical power blackout caused by a terrible geomagnetic storm (Allen et al. 1989). One of the largest solar flares, named the Carrington flare (Carrington 1859), caused one of the most extreme space weather events in the last 200 yr (Tsurutani et al. 2003; Hayakawa et al. 2019), leading to a failure of telegraph systems in Europe and North America (Loomis 1861). The possibility of much more extreme solar storms in a history of solar activity over $\sim$1000 yr has also been recently discussed from cosmogenic isotope measurements and low-latitude auroral drawings (e.g., Miyake et al. 2012, 2013, & 2019; Hayakawa et al. 2017b, 2017a; Usoskin 2017). Thus, it is

---

[8] JSPS Overseas Research Fellow.
[9] JSPS Research Fellow DC1.

[10] We note here for reference that superflares on solar-type stars have been recently reported not only with Kepler and TESS (optical photometry in space) but also with X-ray space telescope observations (e.g., Pye et al. 2015), UV space telescope observations (e.g., Brasseur et al. 2019), and ground-based photometric observations (e.g., Jackman et al. 2018), though currently, the number of observed events is much smaller than the Kepler and TESS results.

important to study the superflares on solar-type stars, especially Sun-like stars (MS stars with surface effective temperature T_{eff} of 5600–6000 K and rotation periods P_{rot} of more than 20 days), and investigate whether our Sun can really generate superflares or not (Shibata et al. 2013; Aulanier et al. 2013; Schmieder 2018; Battersby 2019). Superflares can also affect the climate and habitability of various planets (e.g., Airapetian et al. 2016, 2020; Kay et al. 2019; Yamashiki et al. 2019), and it is important to know how the superflare activities of the Sun and stars change over the stellar age.

A lot of statistical properties of superflares on solar-type stars have recently been revealed through the analysis of the high-precision photometric data of Kepler and the follow-up spectroscopic observations using the Subaru and APO 3.5 m telescopes. The details of these latest results, which are summarized in the following, are described in Notsu et al. (2019):

(i) High-dispersion spectroscopic observations of solar-type superflare stars show that more than half of their observed superflare stars are single solar-type stars (Notsu et al. 2015a, 2019). This suggests that stars having spectro-scopic properties similar to the Sun can generate superflares (see also Nogami et al. 2014).

(ii) The occurrence frequency of superflares as a function of the flare energy on solar-type stars shows a power-law distribution $dN/dE \propto E^{-1.5 \sim -1.9}$, and this is consistent with that of solar flares (Maehara et al. 2012, 2015; Shibayama et al. 2013). This power-law distribution is also confirmed by Tu et al. (2020) using TESS data.

(iii) The superflare stars show quasiperiodic brightness variations with a typical amplitude of 0.1%–10%. These variations are assumed to be explained by the rotation of the stars with large starspots (Notsu et al. 2013b; Maehara et al. 2017; Reinhold et al. 2020). These assumptions are confirmed by spectroscopic observations (Notsu et al. 2015b, 2019; Karoff et al. 2016). The occurrence frequency of starspot size derived from these variations is consistent with that of sunspots, indicating the common generation process of spots (Maehara et al. 2017; Notsu et al. 2019). Also, the temporal evolution of these large starspots is found to be explained by the same process as sunspots (Namekata et al. 2019, 2020a).

(iv) Superflare energies are consistent with the stored magnetic energy estimated from the starspot coverage, indicating that the superflares release magnetic energy around large starspots (Notsu et al. 2013b & 2019). Also, the timescale of the superflares is explained by the magnetically driven energy-release mechanism (i.e., magnetic reconnection; Maehara et al. 2015; Namekata et al. 2017).

(v) Superflares with up to 5×10^{34} erg can occur on slowly rotating Sun-like stars (T_{eff} = 5600–6000 K, $P_{rot} \sim 25$ days, and age ~ 4.6 Gyr) once every few thousand years. In contrast, young rapidly rotating stars with $P_{rot} \sim$ a few days have superflares up to 10^{36} erg, and the flare frequency of such rapidly rotating stars is $\gtrsim 100$ times higher compared with the above old, slowly rotating Sun-like stars (Notsu et al. 2019).

These results have clarified a lot of properties of superflares on Sun-like stars, and we have shown some insights into the important question of whether our Sun can have superflares. However, there remains a large problem: the number of slowly rotating Sun-like superflare stars (T_{eff} = 5600–6000 K and $P_{rot} \sim 25$ days) in Notsu et al. (2019) is very small for the following reasons. Notsu et al. (2019) only used the data originally found as solar-type superflare stars from Kepler 30 minute (long) time cadence data of the first ~ 500 days in Shibayama et al. (2013). The Kepler prime mission continued for 4 yr, so remained the data of ~ 1000 days which were not used in the previous studies. Moreover, Notsu et al. (2019) only investigated superflare stars that are identified as solar-type (G-type MS) stars both in the original Kepler input catalog (Brown et al. 2011) and in the updated Gaia Data Release 2 (DR2) catalog (Berger et al. 2018), since they applied Gaia-DR2 stellar radius updates to superflare stars originally reported in Shibayama et al. (2013) in order to remove contamination of subgiant stars. Thus, a certain number of stars newly identified as solar-type stars in the updated Gaia-DR2 catalog (Berger et al. 2018) are not included for statistical discussions of superflare stars in Notsu et al. (2019). In summary, the statistical survey of superflares with Kepler 4 yr primary data was not completed, and we needed to conduct further statistical analysis of solar-type stars using the full data set of the Kepler primary mission in order to increase the number of Sun-like superflare stars and reveal their statistical properties.

In this study, we searched for superflares using all of the 30 minute (long) time cadence data of the Kepler primary mission covering ~ 1500 days, including the targets newly identified as solar-type stars in the Gaia-DR2 catalog (Berger et al. 2018). Through this, we aim to create a complete catalog of superflares on solar-type stars using Kepler primary mission data and show more well-established results on the properties of superflare stars. In Section 2, we describe the method of analysis, and in Section 3.1, we show the detected superflares on solar-type stars (in Appendix C, we also briefly show and discuss superflares on subgiants). The flare detection method is based on the ones in Shibayama et al. (2013) and Maehara et al. (2015) but not completely the same as them. We use a high-pass Butterworth filter to remove the stellar rotation signals so that we can detect smaller flares in rapidly rotating stars. The processes of removing rotation signals for flare detection are done in many studies (e.g., Davenport et al. 2014). Using these detected superflares, we discuss the latest view on the statistical properties of superflares on solar-type stars in Sections 3.2–3.9. Different from the previous studies, we also include the effect of gyrochronology and sensitivity of flare detection when discussing flare frequency distributions in Sections 3.7 and 3.8.

2. Method

2.1. Data and Analysis

We searched for superflares using the Kepler 30 minute (long) time cadence data (Koch et al. 2010) that were taken from 2009 May to 2013 May (quarters 0–17). We retrieved the data of the Kepler Date Release 25 (DR25; Thompson et al. 2016) from the Multimission Archive at the Space Telescope (MAST). We selected solar-type (G-type MS stars) stars based on the evolutionary state classification and effective temperature (T_{eff}) values listed in Berger et al. (2018). Berger et al. (2018) is the catalog of the 177,911 Kepler stars combining new stellar radius estimates (R_{Gaia}) from Gaia-DR2 parallaxes with the stellar parameters from the DR25 Kepler Stellar Properties Catalog (DR25-KSPC; Mathur et al. 2017), which incorporates the revised method of T_{eff} estimation (Pinsonneault et al. 2012).

Table 1
The Number of Superflares (N_{flare}), Superflare Stars ($N_{flarestar}$), and All Stars We Analyzed (N_{star})

	N_{flare}	$N_{flarestar}$	N_{star}
(1) All Kepler stars having T_{eff} and R_{Gaia} values in Berger et al. (2018)			177,911
(2) All solar-type stars (MS stars with T_{eff} = 5100–6000 K)			49,305
(3) Solar-type stars that have P_{rot} and Amp values reported in McQuillan et al. (2014)	2341 (2344)	265 (266)	11,601
(4) Stars with T_{eff} = 5100–5600 K among item (3)	1412	148	6527
(5) Stars with T_{eff} = 5600–6000 K among item (3)	929 (932)	117 (118)	5074
(6) Sun-like stars (T_{eff} = 5600–6000 K and P_{rot} > 20 days) among item (5)	26 (29)	15 (16)	1641

Note. The T_{eff} values and evolutionary state classifications (MS/subgiants/red giants/cool MS binaries) in Berger et al. (2018; see their Figure 5) are used for the classification in this table. The P_{rot} values in McQuillan et al. (2014) are used for the classification of Sun-like stars in item (6). The number in parentheses includes one superflare star, KIC 007772296, which is suspected as a binary candidate in Table 2 and is not used in the main statistical discussions of this paper (after Section 3.2).

They reported the evolutionary state classifications (MS/ subgiants/red giants/cool MS binaries) on the basis of these R_{Gaia} and T_{eff} values (see Table 5 of Berger et al. 2018). Using the values in Berger et al. (2018), we identified the MS stars with T_{eff} = 5100–6000 K as solar-type stars. In total, 49,305 solar-type stars are selected (see item (2) in Table 1). Among these, 11,601 stars with brightness variation amplitude (Amp) and rotation period (P_{rot}) values reported in McQuillan et al. (2014; see item (3) in Table 1) are finally used for the flare search process.

There are various methods of detecting flares from light curves (e.g., Shibayama et al. 2013; Davenport et al. 2014; Günther et al. 2020). In this study, we follow the flare detection method that is based on our previous studies (Maehara et al. 2012 & 2015; Shibayama et al. 2013), but we include some updates by referring to the methods in several studies (e.g., Gao et al. 2016; Yang et al. 2017). The advantage of the following method is that we do not need to assume any models of flare light-curve shapes to detect flares. Because of this, it is expected that we can detect most of the flares even if they have complicated shapes (e.g., a flare with multiple peaks) in the light curve.

Stellar rotation, which causes periodic variation in light curves, can prevent us from adequately detecting smaller flares (see Yang et al. 2017; Davenport et al. 2020; Feinstein et al. 2020). In particular, this effect becomes larger for detecting flares on rapidly rotating stars ($P_{rot} \sim 1$ day), since the timescales of flares approximately equal the rotation periods. In order to reduce this rotation effect, we use a high-pass Butterworth filter. The passband edge frequency (W_p) is $2 \times 1/P_{rot}$, and the stop-band edge frequency (W_s) is $3 \times 1/P_{rot}$. If P_{rot} is smaller than 0.2 days, we set $W_p = 2 \times 1/0.2$ and $W_s = 3 \times 1/0.2$ day^{-1}, because the high-pass filter does not work. After the light curves are corrected with the high-pass filter method, we calculate the distributions of brightness variations between all pairs of two consecutive data points, as done in our previous studies (e.g., Shibayama et al. 2013). We use this distribution for the flare detection. The threshold of the flare detection was determined as in the to be three times the value at the value of the top 1% of this distribution (1% × 3). In more detail, first we calculated the value A with this criteria: if flux difference is larger than A, the data point is included in the top 1% distribution. Then, we define the flare detection threshold as $A \times 3$. This threshold was chosen as a result of test runs so as not to falsely detect other brightness variations. We also use this to define the end time of the flare.

Figure 1 shows an example of our flare detection method using the light-curve data of KIC 003836772. The rotation period of this star is ~0.6 days. Figure 1(a) is an original light

curve without the high-pass filter, and panel (b) is the distribution of brightness variations between consecutive data points. Figures 1(c) and (d) are the same as panels (a) and (b) but with the high-pass filter. Red arrows (labeled "threshold") in panels (b) and (d) show the threshold (1% × 3) in the distribution, and they are also shown as red bars in panels (a) and (c). Black arrows (labeled "flare") in panels (b) and (d) indicate the maximum flux difference between two consecutive points during the flare shown in panels (a) and (c). Although the flare amplitudes in panels (a) and (c) are almost equal, the "threshold" value in panel (c) is smaller than that in panel (a), thanks to the high-pass filter. Without the high-pass filter, this flare is not detected as a flare, since the "threshold" value (red arrow in panel (b)) is smaller than the maximum flux difference during a flare (black arrow in panel (a)). As shown in this example, this high-pass filter method can help us to not overlook or falsely detect flares. However, since the rotational modulations are not completely removed, the detection threshold of flares can still be affected by the rotational modulations. In particular, rapidly rotating stars tend to have larger effects, and we discuss this point again in Section 3.6.

The flare start time is defined as the time 30 minutes before the flux first exceeds the detection threshold, considering that the time cadence of the Kepler data used here is 30 minutes. We removed long-term brightness variations around the flare by fitting with the spline curves of three points in order to determine the flare end time. Three points are determined by the data points just before the beginning of the flare and 5 and 8 hr after the peak of the flare. The flare end time was determined by the time the flux residuals become smaller than the standard deviation of the distribution (σ_{diff}). Two consecutive data points must exceed the threshold so that the event is defined as a flare. We also excluded flare candidates with a shorter decline phase than the increase phase. This is because most light curves of general stellar flares in the optical show the impulsive brightness increase phase and subsequent, more gradual decrease phase (e.g., the "classical flares" shown in Figure 4 of Davenport et al. 2014). It has been reported that short-duration near-ultraviolet (NUV) flares show different shapes of light curves (e.g., flares whose brightness increase time is comparable to or shorter than the decay time), but the total duration is less than few minutes (Brasseur et al. 2019). We can assume it is almost impossible to detect these short-duration flares with the Kepler 30 minute time cadence data used in this study, though we need more studies on the detailed physical properties of these short-duration flares. Because of these things, we exclude flare candidates with a shorter decline phase than increase phase, considering that these events are
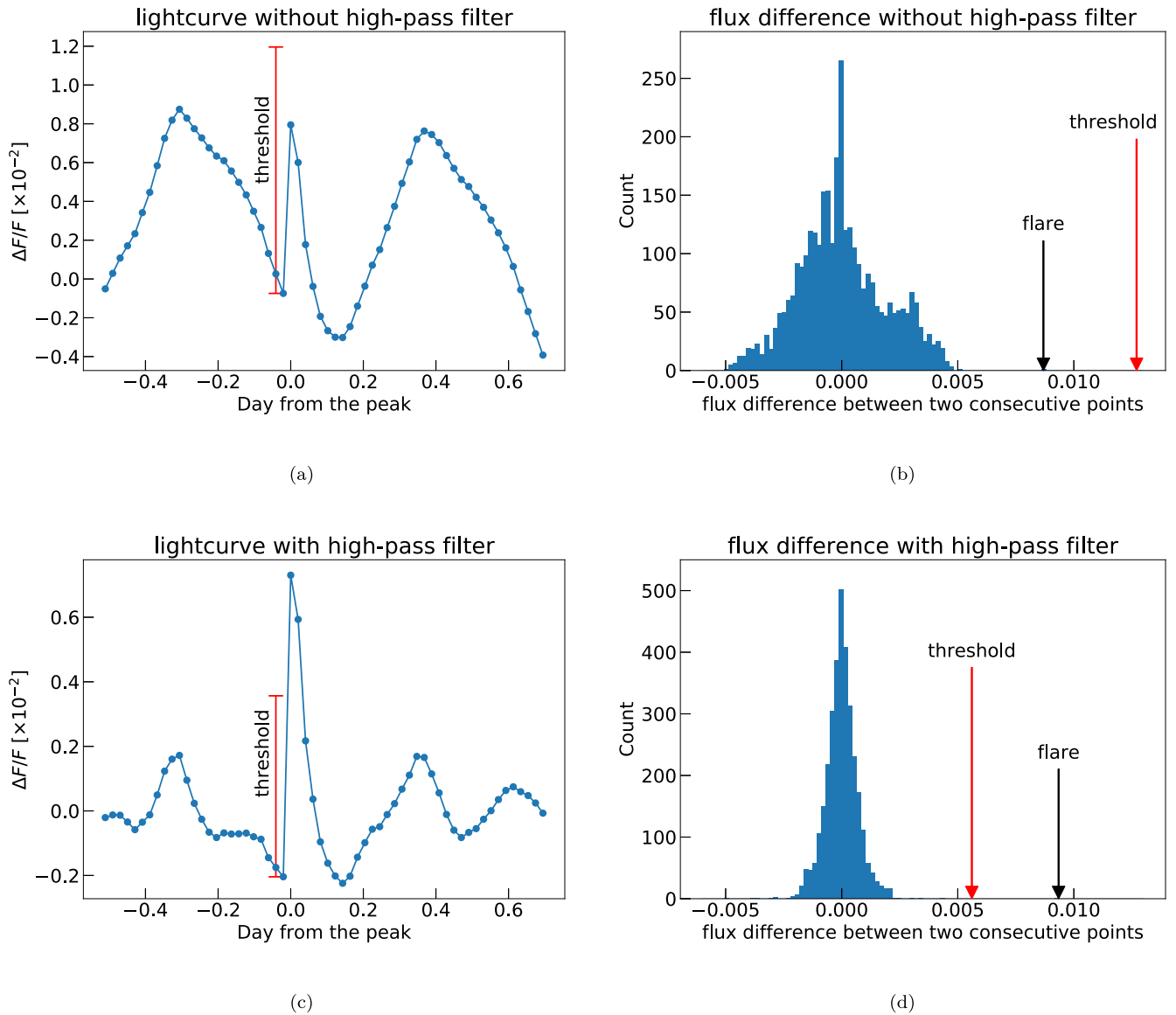
Figure 1. Explanatory figures of our flare detection method using the light-curve data of KIC 003836772. (a) Original light curve without high-pass filter. (b) Distribution of brightness between all pairs of data points in panel (a). (c) Filtered light curve with high-pass filter. (d) Same as panel (b) but the data for panel (c). The threshold of the flare detection was determined to be three times the value at the value of the top 1% of this distribution (1% × 3). In more detail, first we calculated the value A with this criteria: if flux difference is larger than A, the data point is included in the top 1% distribution. Then, we define the flare detection threshold as $A \times 3$. Red arrows (labeled "threshold") in panels (b) and (d) show the above threshold (1% × 3) in the distribution, and they are also shown as red bars in panels (a) and (c). Black arrows (labeled "flare") in panels (b) and (d) indicate the maximum flux difference between two consecutive points during a flare.

caused by instrumental effects or unknown astrophysical events different from flares on solar-type stars.

The pixel scale of the Kepler CCDs is around 4″, and the typical photometric aperture for a 12 mag star is about 30 pixels (Van Cleve & Caldwell 2016). This brightness variation of neighboring stars can affect the flux of the target star, and we removed this effect as done in Shibayama et al. (2013) and Maehara et al. (2015). If a flare star is near the target and large-amplitude flares occur, Kepler will detect fake flares on the target star. To eliminate such events, we chose stars without neighbor stars within 12″ for the analysis using the Kepler Input Catalog. We also excluded pairs of flares that occurred at the same time, and the distance between the flares is less than 24″. By this selection, ∼64% of the detected superflares were excluded. We note here as a caution that it is still possible that there remain some faint stars (>19–20 mag,

fainter than the typical limiting magnitude of the Kepler Input Catalog), even after this selection process. After eliminating the candidates of flares on neighboring stars, we checked the light curves of the flare candidates by eye. Finally, we checked the flux-weighted centroid of the flares in order to investigate whether the flux-weighted centroid in the quiescent phase and the flare phase are the same. If the difference of the flux-weighted centroid at the time of the flare is 3 times larger than the standard deviation of the difference of 10 moving averages, we judge that the flare does not occur on the target star. We compared the periodic flux-weighted centroid moving with periodic light-curve amplitudes of the targets in order to eliminate binaries. If the correlation coefficient of consecutive data points of brightness variation and the flux-weighted centroid is more than 0.5, we eliminated the targets from our flare detection.

2.2. Flare Energy Estimation

We use the methods described in Shibayama et al. ([2013](#)) to estimate the total energy of each flare. We assumed that the spectrum of white-light flares can be described by blackbody radiation with an effective temperature (T_{flare}) of 10,000 K (Mochnacki & Zirin [1980](#); Hawley & Fisher [1992](#)). Assuming that the star is a blackbody radiator, the relationship between the bolometric flare luminosity (L_{flare}), the flare effective temperature (T_{flare}), and the area of the flare (A_{flare}) is written as the following equation with the Stefan–Boltzmann constant (σ_{SB}):

$$L_{\mathrm{flare}} = \sigma_{\mathrm{SB}} T_{\mathrm{flare}}^4 A_{\mathrm{flare}}. \tag{1}$$

We estimate A_{flare} with the observed luminosity of the star (L'_{star}) and flare (L'_{flare}) using Equations (2)–(5) of Shibayama et al. ([2013](#)). The total bolometric energy of the superflare (E_{flare}) is written as an integral of $L_{\mathrm{flare}}(t)$ during the flare duration,

$$E_{\mathrm{flare}} = \int_{\mathrm{flare}} L_{\mathrm{flare}}(t)\,dt. \tag{2}$$

This estimate of E_{flare} is affected by several types of uncertainties. Errors of stellar effective temperature (T_{eff}) and stellar radius (R) affect E_{flare} values, and these are typically $\sim3\%$ and $\sim7\%$, respectively (Berger et al. [2018](#)). The determination errors of flare start/end points and quiescent levels also have effects on flare amplitude values and, consequently, E_{flare} values (typically $\sim30\%$). If the blackbody temperature of a flare emission changes to 6000–7000 K, as in solar white-light flares, the flare energy can change by a factor of 0.5 (Namekata et al. [2017](#)). Moreover, since both stellar quiescent radiation and flare emission may not be complete blackbody radiation, E_{flare} values may have an error of a few tens of percent. In total, E_{flare} values can have error values of a few tens of percent. We must note these potential error values when we discuss the exact E_{flare} values reported in the following sections. However, the overall statistical discussions of the relations between superflares and stellar properties (e.g., rotation period, starspot coverage) do not change, since the errors are smaller than 1 order of magnitude.

3. Results and Discussion

3.1. Detected Superflares

We detected 2344 superflares on 266 solar-type stars from Kepler 30 minute (long) time cadence data of ~4 yr (quarters 0–17). Among them, we detected 29 superflares on 16 Sun-like stars ($T_{\mathrm{eff}} = 5600$–6000 K and $P_{\mathrm{rot}} > 20$ days). The number of superflares (N_{flare}), superflare stars ($N_{\mathrm{flarestar}}$), and all stars analyzed (N_{star}) are listed in Table [1](#). The sample size (the number of stars × observation period) of solar-type stars in this study is about four times larger than that of Notsu et al. ([2019](#)), and the sample size on Sun-like stars is about 12 times larger. The number of superflares on Sun-like stars detected in this study is >12 times larger than Notsu et al. ([2019](#)), since we improved the methods to detect superflares (Section [2.1](#)). We note again that our previous study, Notsu et al. ([2019](#)), did not include stars newly identified as solar-type stars in the updated Gaia-DR2 catalog (Berger et al. [2018](#)). Notsu et al. ([2019](#)) applied Gaia-DR2 stellar radius values only to the stars that had been identified as solar-type stars in Shibayama et al. ([2013](#)), which used the original Kepler input catalog (Brown et al. [2011](#)) for selecting solar-type stars. The effective temperature

in the original Kepler input catalog (Brown et al. [2011](#)) is about 250 K lower than that in the Gaia-DR2 catalog (Berger et al. [2018](#)) for most solar-type stars. This is the main reason why the sample increase of Sun-like stars ($T_{\mathrm{eff}} = 5600$–6000 K and $P_{\mathrm{rot}} > 20$ day) is 12 times, while that of solar-type stars ($T_{\mathrm{eff}} = 5100$–6000 K) is only four times.

The stellar and flare parameters of all Sun-like superflare stars detected in this study are listed in Table [2](#). The data of all 2344 superflares on 266 solar-type superflare stars detected in this study are available in the online-only table. Some example light curves of superflares on the Sun-like stars are shown in Figure [2](#), and all superflares on Sun-like stars are shown in Appendix [A](#). In addition to superflares on solar-type (G-type MS) stars, we also detected superflares on subgiants, and these are briefly shown and discussed in Appendix [C](#).

It is generally difficult to accurately detect rotation period values of stars as slow as the Sun ($P_{\mathrm{rot}} > 20$ days), so we double-checked the rotation periods of all of the Sun-like superflare stars (detailed in Appendix [A](#)). As a result, some stars may have rotation period values smaller than the values reported in McQuillan et al. ([2014](#)). These five stars are flagged as "1" in Table [2](#), while they are used in the statistical discussions in the following part of this paper because we cannot finally judge only from the periodogram analyses in Appendix [A](#). Flagged as "2" in Table [2](#), KIC 007772296 is suspected as a binary candidate. The light-curve and periodogram analyses suggest that this star also shows brightness variations with a period of ~1 day, and this short period might be related to the orbital motion of a binary system (for details, see Appendix [A](#)). Because of this, KIC 007772296 is not used in the statistical discussions in the following part of this paper. We also note again that it is still possible that there remain some faint stars (>19–20 mag) in the Kepler photometric aperture ($12''$). As a result of this paper, we detected 2341 superflares on 265 solar-type stars, and among them, we detected 26 superflares on 15 Sun-like stars ($T_{\mathrm{eff}} = 5600$–6000 K and $P_{\mathrm{rot}} > 20$ days). These superflare stars are used in the statistical discussions in the following part of this paper.

3.2. Dependence of Superflare Energy on Rotation Period

Previous survey observations of stellar activity levels (e.g., X-ray-quiescent luminosity, Ca II H and K index) have shown that the stellar magnetic level decreases as rotation period increases (Noyes et al. [1984](#); Güdel [2007](#); Wright et al. [2011](#)). Since stellar age has a strong correlation with rotation, young rapidly rotating stars show higher activity levels, and slowly rotating stars, like the Sun, show lower activity levels. Following this, we expected superflare activities to depend on the rotation period. Notsu et al. ([2019](#)) suggested that the maximum superflare energy continuously decreases as the rotation period increases, and there is a difference of roughly 1 order of magnitude between the maximum flare energy on rapidly rotating stars ($P_{\mathrm{rot}} \sim$ a few days) and slowly rotating stars ($P_{\mathrm{rot}} > 20$ days). However, a large problem remains: there were some uncertainties on the upper limit of flare energy on Sun-like ($T_{\mathrm{eff}} = 5600$–6000 K and $P_{\mathrm{rot}} > 20$ days) stars because the number of Sun-like superflare stars in Notsu et al. ([2019](#)) was very small.

We then investigated this relation using a much larger number of superflares newly detected in this study (e.g., an ~12 times larger sample of Sun-like stars, as described in Section [3.1](#)). Figure [3](#) shows the relationship between the flare energy (E_{flare}) and the rotation period (P_{rot}). The data of the stars with a temperature range ($T_{\mathrm{eff}} = 5600$–6000 K) close to

Table 2
Parameters of Sun-like Superflare Stars

KIC	$T_{\rm eff}$[a] (K)	R[a] ($R_\odot$)	$P_{\rm rot}$[c] (days)	Amp[c] (ppm)	$m_{\rm Kepler}$[d] (mag)	$N_{\rm flare}$[e]	$E_{\rm max}$[e] (erg)	$A_{\rm spot}$[f] ($1/2 \times A_\odot$)	Flag[g]
005648294	5653 ± 198	$1.140^{+0.091}_{-0.082}$	22.336 ± 0.085	2543.81	14.757	1	2.4×10^{34}	4.3×10^{-3}	1
005695372	5791 ± 203	$0.886^{+0.066}_{-0.060}$	21.195 ± 0.130	8881.39	14.054	3	7.7×10^{33}	8.9×10^{-3}	...
0063476560[b]	5623 ± 197	$0.823^{+0.062}_{-0.057}$	28.441 ± 0.598	4110.04	14.860	4	2.2×10^{34}	3.6×10^{-3}	1
006932164	5731 ± 201	$1.038^{+0.104}_{-0.093}$	22.631 ± 0.077	8538.25	15.883	1	4.0×10^{34}	1.3×10^{-2}	...
007435701	5812 ± 203	$0.809^{+0.063}_{-0.057}$	20.648 ± 0.053	8039.18	15.090	1	9.1×10^{33}	6.7×10^{-3}	...
007772296	5616 ± 197	$0.897^{+0.070}_{-0.063}$	23.257 ± 0.083	4136.53	14.880	3	1.1×10^{34}	4.3×10^{-3}	2
007886115	5729 ± 201	$0.873^{+0.066}_{-0.060}$	20.351 ± 0.110	5280.17	14.960	1	9.0×10^{33}	5.2×10^{-3}	...
008090349	5760 ± 202	$1.169^{+0.092}_{-0.083}$	24.898 ± 3.822	2482.89	14.675	1	1.8×10^{34}	4.4×10^{-3}	...
008416788	5889 ± 206	$0.908^{+0.068}_{-0.061}$	22.519 ± 0.042	3300.19	13.582	5	1.7×10^{34}	3.4×10^{-3}	...
009520338	5947 ± 208	$0.805^{+0.064}_{-0.058}$	23.857 ± 0.093	4138.47	15.270	1	9.9×10^{33}	3.4×10^{-3}	1
010011070[b]	5669 ± 198	$0.770^{+0.059}_{-0.053}$	23.970 ± 0.623	4423.92	14.949	2	1.6×10^{34}	3.4×10^{-3}	...
010275962	5782 ± 202	$0.789^{+0.064}_{-0.058}$	26.117 ± 1.426	2323.69	15.296	2	1.9×10^{34}	1.9×10^{-3}	1
011075480	5953 ± 208	$0.795^{+0.063}_{-0.057}$	21.651 ± 0.278	2001.46	15.108	1	9.3×10^{33}	1.6×10^{-3}	...
011141091	5756 ± 201	$0.879^{+0.068}_{-0.062}$	23.446 ± 0.373	2345.32	14.982	1	1.5×10^{34}	2.3×10^{-3}	...
011413690	5886 ± 206	$0.818^{+0.069}_{-0.062}$	24.238 ± 0.246	3232.87	15.725	1	3.0×10^{34}	2.7×10^{-3}	1
012053270	5971 ± 209	$0.744^{+0.058}_{-0.053}$	21.796 ± 1.587	4338.80	15.017	1	3.1×10^{34}	3.0×10^{-3}	...

Notes. The data of the 2344 superflares on the 266 solar-type superflare stars detected in this study are available in the online-only table.
[a] Effective temperature and stellar radius values are taken from Gaia-DR2 in Berger et al. (2018). Stellar radii are shown in units of solar radius ($R_\odot$).
[b] These two stars are also reported in Notsu et al. (2019). See further details in Appendix B.
[c] The rotation periods and average rotational variability are reported in McQuillan et al. (2014).
[d] Kepler-band magnitude (Thompson et al. 2016).
[e] Here $N_{\rm flare}$ and $E_{\rm max}$ are the number of superflares and maximum energy of superflares of each Sun-like star, respectively.
[f] Area of the starspots on each Sun-like star in units of the area of the solar hemisphere ($1/2 \times A_\odot \sim 3 \times 10^{22}$ cm^2).
[g] Flag 1: It is possible that the real rotation period value of the star is different from those reported in McQuillan et al. (2014) and used in this table on the basis of our extra analyses (see Appendix A and Figures 16 and 19 therein). Then the rotation period value of these stars should be treated with caution, and it is possible that some of these stars are not really Sun-like stars, though more investigations are needed (see Appendix A for details). Flag 2: This star is suspected to have a binary (see Figures 17 and 20 in Appendix A). This star is not used in the statistical discussions after Section 3.3.

(This table is available in its entirety in machine-readable form.)

the solar temperature ($T_{\rm eff} \sim 5800$ K) are plotted with red open squares, while those of late G-type MS stars ($T_{\rm eff} = 5100$–5600 K) are blue plus signs. Similar to the results of Notsu et al. (2019), the upper limit of $E_{\rm flare}$ in each period bin has a continuous decreasing trend with the rotation period. There is at least an order-of-magnitude difference between the maximum flare energy on rapidly rotating stars ($P_{\rm rot} \sim$ a few days) and slowly rotating stars ($P_{\rm rot} > 20$ days). This decreasing trend, which is confirmed in Notsu et al. (2019) and this study, was not reported in our initial study, Notsu et al. (2013b). This is because some fraction ($\sim 40\%$) of superflare stars in our initial studies (Maehara et al. 2012; Shibayama et al. 2013; Notsu et al. 2013b) are now found to be subgiants (Notsu et al. 2019), and this contamination of subgiants affected the statistics (see Appendix C for details).

In Figure 3, we added the stellar age (t) using the gyrochronological relation ($P_{\rm rot} \propto t^{0.6}$; Ayres 1997)[11] for $T_{\rm eff} = 5600$–6000 K in order to compare the age of the superflare stars with that of the Sun ($t \sim 4.6$ Gyr). With this scale, as a result of Figure 3, we confirm again that old, slowly rotating Sun-like stars ($T_{\rm eff} = 5600$–6000 K, $P_{\rm rot} > 20$ days, and age ~ 4.6 Gyr) can have superflares with $\lesssim 4 \times 10^{34}$ erg, while young, rapidly rotating stars have superflares with up to $\sim 10^{36}$ erg. The scale of t is only plotted in the limited age range $t = 0.5$–5 Gyr for the following two reasons. (1) As for young solar-type stars

with $t \lesssim 0.5$–0.6 Gyr, a large scatter in the age–rotation relation has been reported from young cluster observations (e.g., Soderblom et al. 1993; Ayres 1997; Tu et al. 2015). (2) As for old solar-type stars beyond the solar age ($t \sim 4.6$ Gyr), a breakdown of the gyrochronology relations was recently suggested (van Saders et al. 2016; Metcalfe & Egeland 2019).

We note that in Figure 3, there is an apparent negative correlation between the rotation period and the lower limit of the flare energy. However, this trend only reflects the detection limit affected by the rotation period, as discussed in Section 3.6. We also note that in Figure 3, the sample size of the stars in each $P_{\rm rot}$ bin is different. The number of samples of slowly rotating stars is larger than that of rapidly rotating stars. It is then possible that rare energetic flares approaching the upper limit value for each $P_{\rm rot}$ bin can be a bit more easily detected on slowly rotating stars than rapidly rotating stars, assuming the power-law flare frequency distributions shown in Section 3.7. This might be related to the tendency that the upper limit of flare energy is roughly constant in the range of $P_{\rm rot} > 10$ days. For the same reason, the upper limit $E_{\rm flare}$ value of rapidly rotating stars ($P_{\rm rot} < 20$ days) can be a bit larger ($> 10^{36}$ erg). We will discuss this point in more detail, together with the flare frequency distributions, in Section 3.7.

3.3. Starspot Size and Superflare Energy

Most superflare stars show large-amplitude brightness variations, and they suggest that the surfaces of superflare stars are covered by large starspots. Figure 4 shows a scatter plot of flare

---

[11] We note here that the relation $P_{\rm rot} \propto t^{0.6}$ was incorrectly written in the text of Notsu et al. (2019; as $t \propto P_{\rm rot}^{0.6}$), though this did not affect on our discussions and conclusions in Notsu et al. (2019), since the figures were plotted correctly.
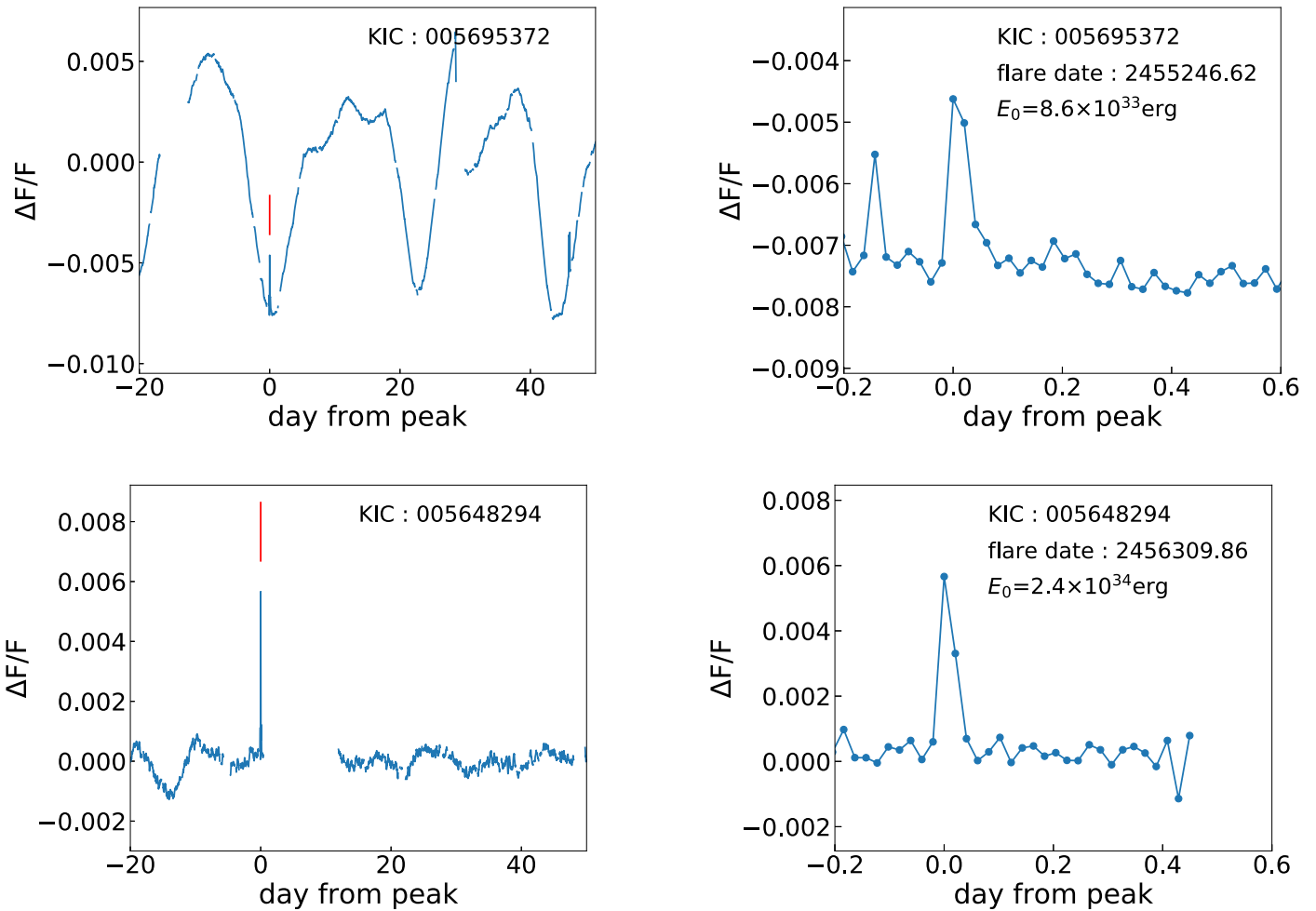
Figure 2. Light curves of the example superflares on Sun-like stars. The horizontal and vertical axes correspond to days from the flare peak and stellar brightness normalized by the average brightness during the observation quarter of Kepler. The panels on the left show the 70 day time variation of stellar brightness to see the periodic brightness variations caused by stellar rotation. The panels on the right show the detailed brightness variations of a flare. The star ID (Kepler ID), Barycentric Julian Date of the flare peak, and released total bolometric energy are shown in the right panels.
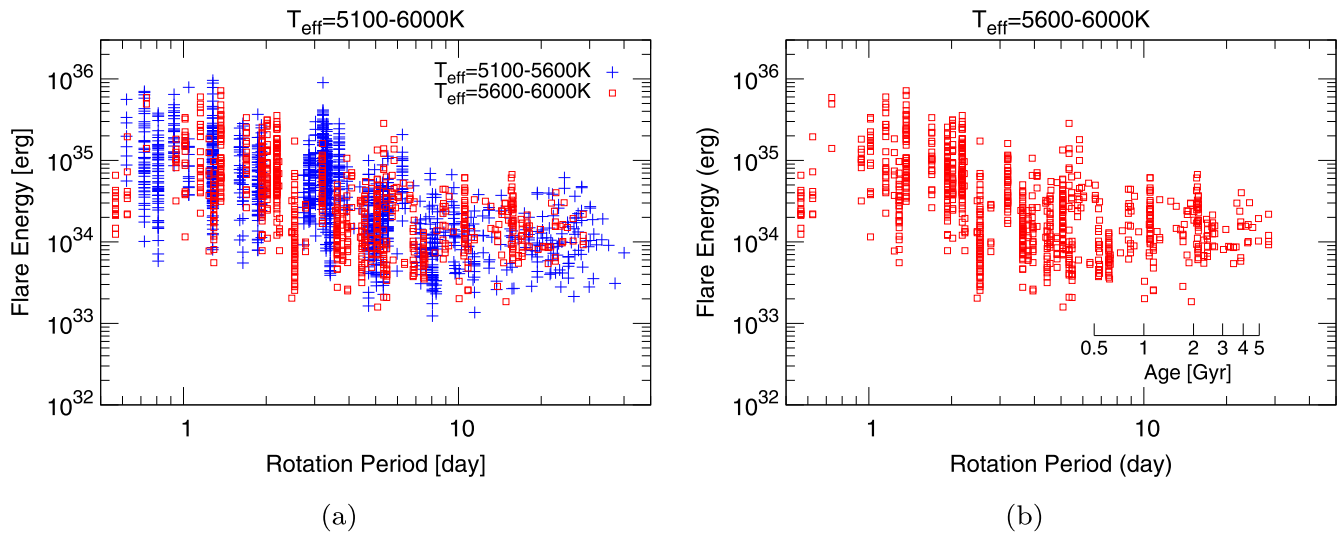
Figure 3. Scatter plot of the superflare energy ($E_{\rm flare}$) vs. the rotation period ($P_{\rm rot}$). Here $P_{\rm rot}$ was estimated from the brightness variation period (McQuillan et al. 2014), and superflares are detected from all of the Kepler 4 yr 30 minute cadence data. Blue plus signs indicate superflares detected on solar-type stars with $T_{\rm eff} = 5100–5600$ K, while red squares are those with $T_{\rm eff} = 5600–6000$ K. For $T_{\rm eff} = 5600–6000$ K in panel (b), we added the scale of stellar age (t) based on the gyrochronology relation of solar-type stars ($P_{\rm rot} \propto t^{0.6}$; Ayres 1997), as also used in the previous study (Notsu et al. 2019). We note that there is an apparent negative correlation between the rotation period and the lower limit of the flare energy, but this trend only reflects the detection limit, and this detection limit is related to the rotation period, as discussed in Section 3.6.
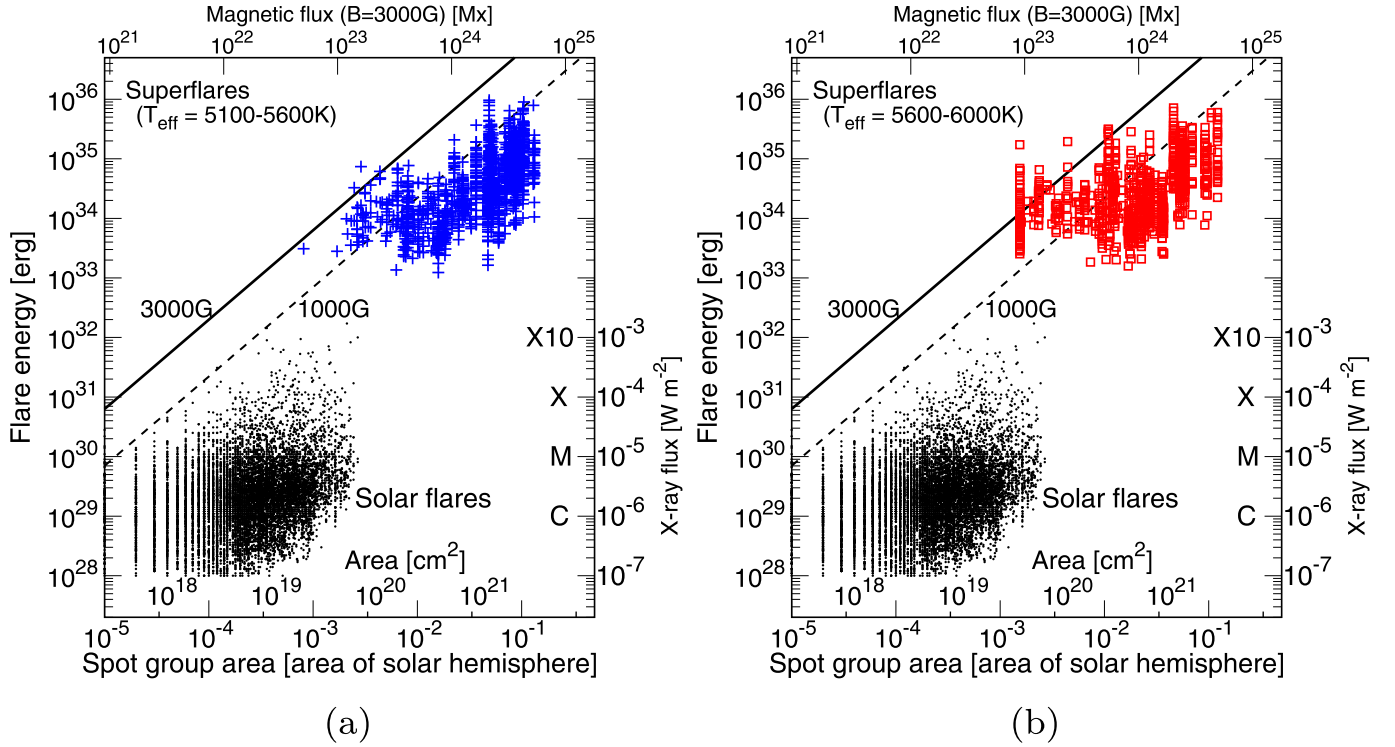
Figure 4. Scatter plot of the superflare energy (E_{flare}) and spot group area (A_{spot}) of solar flares and superflares. The lower and upper horizontal axes show the area of the spot group in unit of the solar hemisphere ($1/2 \times A_\odot \sim 3 \times 10^{22}$ cm^2) and the magnetic flux for $B = 3000$ G. The left vertical axis shows the bolometric energy released by each flare. The data of the solar flares are exactly the same as those in our previous studies (e.g., Figure 6 of Notsu et al. 2019). We assumed that bolometric energies of B-, C-, M-, X-, and X10-class solar flares are 10^{28}, 10^{29}, 10^{30}, 10^{31}, and 10^{32} erg from observational estimates of solar flare energies. The black solid and dashed lines correspond to the relationship between E_{flare} and A_{spot} for $B = 3000$ and 1000 G, respectively; see Equation (4). (a) Superflares on solar-type stars with $T_{\mathrm{eff}} = 5100$–5600 K are shown with blue crosses. (b) Superflares on solar-type stars with $T_{\mathrm{eff}} = 5600$–6000 K are shown with red open squares.

energy (E_{flare}) as a function of the spot group area (A_{spot}) of solar flares and superflare stars. The A_{spot} values are estimated the same way as in our previous studies (Shibata et al. 2013; Notsu et al. 2019). In these studies, we used the following equation (see Equation (3) of Notsu et al. 2019):

$$A_{\mathrm{spot}} = \frac{\Delta F}{F} A_{\mathrm{star}} \left[1 - \left(\frac{T_{\mathrm{spot}}}{T_{\mathrm{star}}} \right)^4 \right]^{-1}, \qquad (3)$$

where A_{star}, T_{spot}, and T_{star} are the apparent area of the star (πR_{star}^2) and the temperature of the starspot and the photosphere, respectively. In this study, T_{eff} values from Berger et al. (2018) are used for T_{star} values. The T_{spot} values are estimated from T_{star} values by using the empirical relation (Equation (4) of Notsu et al. 2019) deduced from Berdyugina (2005). The total energy released by the flare (E_{flare}) must be smaller than (or equal to) the magnetic energy stored around starspots (E_{mag}). Our previous papers (e.g., Shibata et al. 2013; Notsu et al. 2019) suggested that the upper limit of flare energy (E_{flare}) can be determined by the simple scaling law (see Equation (5) of Notsu et al. 2019):

$$E_{\mathrm{flare}} \approx f E_{\mathrm{mag}} \approx \frac{B^2 L^3}{8\pi} \approx 7 \times 10^{32} (\mathrm{erg})$$

$$\times \left(\frac{f}{0.1} \right) \left(\frac{B}{10^3 \mathrm{G}} \right)^2 \left(\frac{A_{\mathrm{spot}}/(2\pi R_\odot^2)}{0.001} \right)^{3/2}, \qquad (4)$$

where f is the fraction of magnetic energy that can be released as flare energy, B and L are the magnetic field strength and size of the spot, and $R_\odot$ is the solar radius. We note that analyses of

large solar flares in Emslie et al. (2012) suggest bolometric flare energies are ∼0.1 of the available magnetic energies (see Figure 4 of Emslie et al. 2012).

In Figure 4, almost all the data points of the superflares are below the line of Equation (4) for $B = 3000$ G, and the upper limit of the flare energies tends to increase as the spot area increases. This means that the superflare is the magnetic energy release stored around the starspots, and the process is the same as that of solar flares. In Figure 5, we also compare the data of Sun-like stars with that of the Sun for reference.

We note that the starspot group area estimated here can be smaller than the actual values if the stars have a low inclination angle or have starspots around the pole region (see also Notsu et al. 2015b & 2019 for details). Besides, the real size of the spot group when a superflare occurs can be larger than the size estimated from the brightness amplitude values, since we only use the time-averaged brightness amplitude (Amp) values reported in McQuillan et al. (2014). Some evolution/decay of starspot coverage, which can occur in a timescale of ∼100 days (e.g., Namekata et al. 2019, 2020a), is time-averaged. These can be the reason why some data points of superflares locate above the line of Equation (4) (for $B = 3000$ G) in Figure 4. As a result, we can conclude that the upper limit of the flare energy is consistent with the magnetic energy stored around the starspots, as also confirmed in Notsu et al. (2019).

3.4. Starspot Size versus Rotation Period of Solar-type Stars and Implications for Superflare Energy

In Section 3.2, we confirmed that the upper limit of the superflare energy has a decreasing trend with rotation period. In
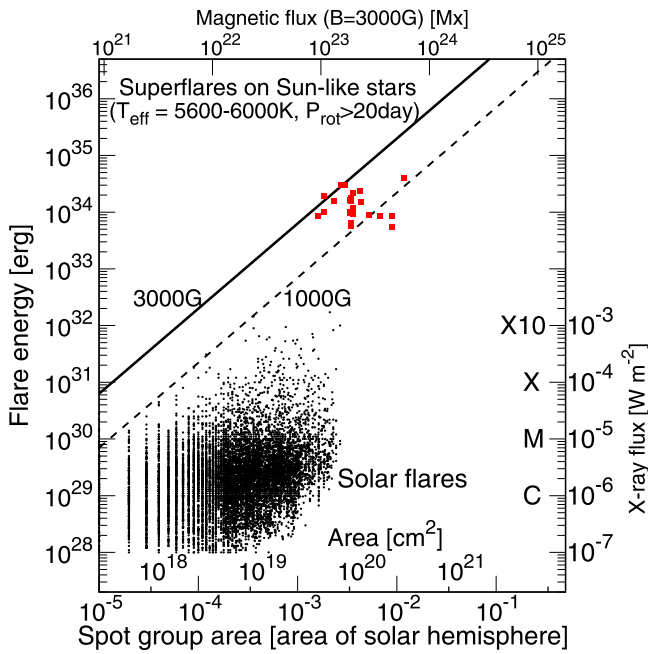
Figure 5. Same as Figure 4, but for Sun-like stars.

Section 3.3, we also confirmed that the upper limit of the flare energy is consistent with the starspot coverage, considering that magnetic energy is stored around starspots. Then, how is starspot coverage related to rotation period, and what implications exist for superflare energy?

Our previous paper, Maehara et al. (2017), investigated the statistical properties of starspots on solar-type stars by using the starspot size (A_{spot}) and rotation period (P_{rot}) estimated from the brightness variations of Kepler data, and Notsu et al. (2019) updated the results by using Gaia-DR2 stellar radius. The resultant values of A_{spot} and P_{rot} are shown in Figure 6, with the increased data of superflare stars newly identified in this paper. As also shown in Notsu et al. (2019), the stars showing more energetic superflares tend to have shorter rotation periods (younger ages) and larger starspot areas.

Figure 6 shows that the largest area of starspots on solar-type stars in a given P_{rot} bin has a roughly constant or very gentle decreasing trend in the period range of $P_{rot} \lesssim 12$ days (age: $t \lesssim 1.4$ Gyr) for the solar-type stars with $T_{eff} = 5600$–6000 K and $P_{rot} \lesssim 14$ days for those with $T_{eff} = 5100$–5600 K. However, in the period range of $P_{rot} \gtrsim 12$ days (age: $t \gtrsim 1.4$ Gyr) for the stars with $T_{eff} = 5600$–6000 K and $P_{rot} \gtrsim 14$ days for those with $T_{eff} = 5100$–5600 K, the largest starspot area of the stars steeply decreases as the rotation period increases. This decreasing trend of the maximum area of the starspots can be related to the decreasing trend of maximum flare energy confirmed in Section 3.2 (see Figure 3). This is because the maximum area of the starspots determines well the upper limit of flare energy, as indicated in Section 3.3. In the case of slowly rotating Sun-like stars with $T_{eff} = 5600$–6000 K and $P_{rot} \sim 25$ days, Figure 6(b) shows that the maximum size of the starspots is a few percent of the solar hemisphere. These values correspond to 10^{34}–10^{35} erg by Equation (4), and the upper limit of the superflare energy of these Sun-like stars in Figure 3 is roughly in the same range.

It is difficult to conclude whether A_{spot} values are constant or decrease in the short period range because of several factors. As

indicated in Section 3.3, the A_{spot} values estimated from the brightness variations can be smaller than the actual values. For example, the A_{spot} values estimated from the brightness variations can be smaller than the actual values if the stars have a low inclination angle or starspots around the pole region (see also Notsu et al. 2015b & 2019). In addition, more active stars, such as rapidly rotating stars, can have multiple starspots on the surface, and this also causes the A_{spot} estimated from the brightness variations to be smaller than the total spot coverage of the star (Namekata et al. 2020a).

However, there is a difference in a bit stricter sense between the decreasing trends of the maximum superflare energy in Figure 3 and the maximum area of the starspots in Figure 6. The maximum superflare energy continuously decreases as the rotation period increases (the star becomes older) in Figure 3, but the maximum area of the starspots does not show such a continuous decreasing trend in Figure 6. On the other hand, the maximum area of the starspots is roughly constant or very gently decreases in the short period range ($P_{rot} \lesssim 14$ days), but it steeply decreases as the period increases in the longer range ($P_{rot} \gtrsim 14$ days). This difference was also suggested in our previous paper, Notsu et al. (2019), but it was not as clear, since the number of superflare events was small. If this difference between the decreasing trends in Figures 3 and 6 is true, there can be a possibility that the flare energy is determined not only by the starspot area but also by other important factors, though the starspot area is still a necessary condition to determine the flare energy (see Section 3.3). Considering the correlation between the flare activity and the magnetic structure of sunspot groups (see Sammis et al. 2000; Toriumi & Wang 2019), one of the possible factors might be the effect of the magnetic structure of starspots. More complex spots can generate more frequent and energetic flares according to solar observations. If the magnetic structure (complexity) of spots also has a correlation with the rotation period, the upper limit of the flare energy can depend on rotation period, even if the starspot size is roughly constant. We need to conduct more detailed studies on starspot properties to clarify such possibilities (e.g., observations using exoplanet transits in Namekata et al. 2020a).

In addition, as suggested in Notsu et al. (2019), the constant and decreasing trends of maximum starspot coverage can be compared with the relation between X-ray flux and rotation period (e.g., Wright et al. 2011). The X-ray fluxes of solar-type stars are also known to show the constant regime (or so-called "saturation" regime) in the period range of $P_{rot} \lesssim 2$–3 days, but they decrease constantly as the P_{rot} values increase in the range of $P_{rot} \gtrsim 2$–3 days. The changing point of this X-ray trend ($P_{rot} \lesssim 2$–3 days) is different from that of maximum spot size values ($P_{rot} \lesssim 12$–14 days). These similarities and differences can be interesting and helpful when considering the relation between stellar activity (including starspots, flares, and X-ray steady emissions) and rotation period in more detail, though a detailed study of this point is beyond the scope of this paper.

3.5. Differences between the Number of Stars Having Rotation Period Values and the Number of Stars in the Kepler Field

In Appendix B of Notsu et al. (2019), we investigated the potential differences between the number of stars with P_{rot} values in McQuillan et al. (2014) and the number of the "real" sample of Kepler field stars by using the gyrochronological relation. As also shown in Table 3, ~69% (=(20,893–6527)/20,893) and ~82% (=(28,412–5064)/28,412) of the solar-type
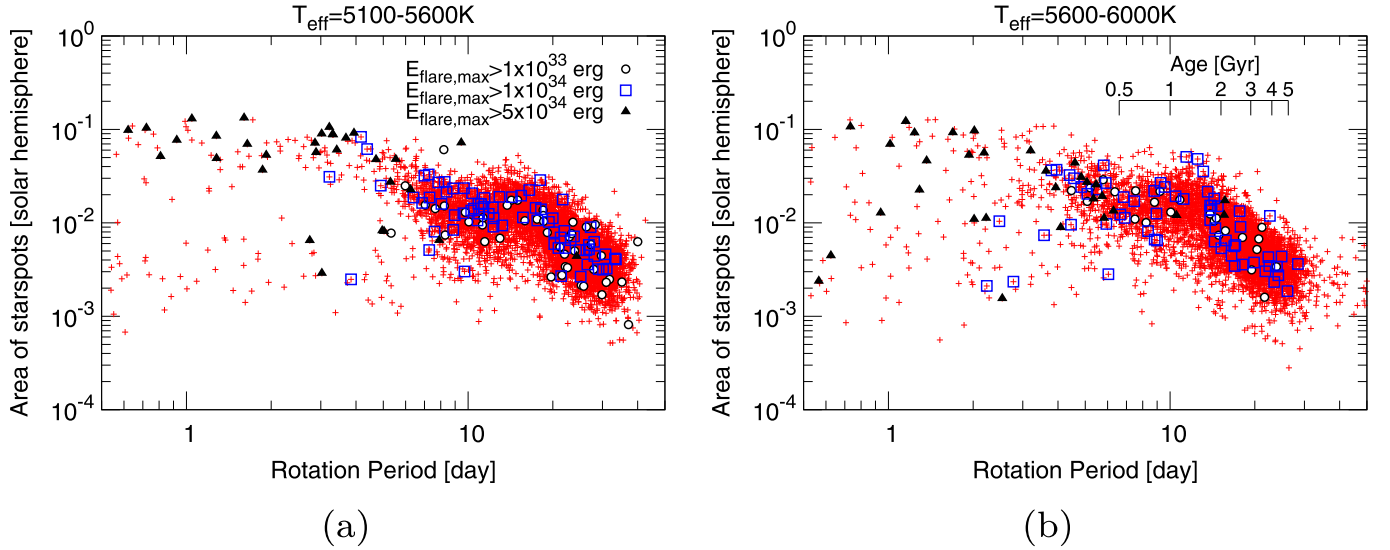
Figure 6. Scatter plot of the spot group area of solar-type stars ($A_{\rm spot}$) as a function of the rotation period ($P_{\rm rot}$). The vertical axis represents $A_{\rm spot}$ in units of the area of the solar hemisphere ($A_\odot \sim 3 \times 10^{22}$ cm^2). Black open circles, blue open squares, and black filled triangles indicate solar-type stars that have superflares with energy values of their most energetic flares of $E_{\rm flare,max} > 1 \times 10^{33}$, 1×10^{34}, and 5×10^{34} erg, respectively. Small red plus signs indicate all solar-type stars. The plotted data are separated on the basis of the temperature values: (a) $T_{\rm eff} = 5100$–5600 K and (b) $T_{\rm eff} = 5600$–6000 K. In panel (b) only, we added the scale of stellar age (t) based on the gyrochronology relation for solar-type stars ($P_{\rm rot} \propto t^{0.6}$; Ayres 1997; see Section 3.2 for details).

Table 3
Differences between the Number of Kepler Solar-type Stars with $T_{\rm eff} = 5100$–5600 and 5600–6000 K that Have $P_{\rm rot}$ Values Reported in McQuillan et al. (2014) and the Number of Field Stars Estimated from the Gyrochronological Relation (See Equation (5))

$T_{\rm eff} = 5100$–5600 K	N_P[a] (Have $P_{\rm rot}$ Values)	$N_{\rm star}$[b] (from Gyrochronology)
All	6527	20,893
$P_{\rm rot} < 5$ days	175 (3%)	221 (1%)
$P_{\rm rot} = 5$–10 days	734 (11%)	620 (3%)
$P_{\rm rot} = 10$–20 days	2235 (34%)	2359 (11%)
$P_{\rm rot} = 20$–40 days	3374 (52%)	17,693 (85%)
$T_{\rm eff} = 5600$–6000 K	N_P[a] (have $P_{\rm rot}$ values)	$N_{\rm star}$[b] (from gyrochronology)
All	5064	28,412
$P_{\rm rot} < 5$ days	314 (6%)	507 (2%)
$P_{\rm rot} = 5$–10 days	785 (16%)	1422 (5%)
$P_{\rm rot} = 10$–20 days	2325 (46%)	5407 (19%)
$P_{\rm rot} = 20$–40 days	1640 (32%)	21,075 (74%)

Notes.
[a] Number of stars that have $P_{\rm rot}$ and Amp values reported in McQuillan et al. (2014).
[b] Number of stars estimated from the gyrochronology relation. The number in the first column corresponds to the number of all Kepler solar-type stars with $T_{\rm eff} = 5100$–5600 and 5600–6000 K (see item (2) in Table 1).

stars with $T_{\rm eff} = 5100$–5600 and 5600–6000 K, respectively, have no $P_{\rm rot}$ values in our sample, and they are not plotted in Figure 6. This is because the brightness variation amplitudes of these "inactive" solar-type stars are smaller than the detection limit. We need to pay attention to biases caused by these "inactive" solar-type stars when discussing the relation between the rotation period and superflare properties, such as the occurrence frequency of superflares. The number of stars having $P_{\rm rot}$ values in each $P_{\rm rot}$ bin of Table 3 does not show the actual $P_{\rm rot}$ distribution of the Kepler field. This is because the

"inactive" stars with no $P_{\rm rot}$ values are expected to be dominated by old, slowly rotating stars, and this can be a big problem, especially for discussing the flare frequencies of slowly rotating stars.

In order to roughly evaluate the potential differences caused by the above points, our previous paper, Notsu et al. (2019), estimated the number fraction of solar-type stars in specific $P_{\rm rot}$ bins by using the empirical gyrochronology relation (Ayres 1997; Mamajek & Hillenbrand 2008). The number of stars with $P_{\rm rot}$ values larger than P_0 ($N_{\rm star}(P_{\rm rot} \geqslant P_0)$) can be estimated from the duration of the MS phase ($\tau_{\rm MS}$), the gyrochronological age of the star ($t_{\rm gyro}(P_0)$), and the total number of stars ($N_{\rm all}$):

$$N_{\rm star}(P_{\rm rot} \geqslant P_0) = \left(1 - \frac{t_{\rm gyro}(P_0)}{\tau_{MS}}\right) N_{\rm all}. \quad (5)$$

We assumed that the star formation rate around the Kepler field has been roughly constant over $\tau_{\rm MS}$.

Using Equations (12)–(14) of Mamajek & Hillenbrand (2008), we roughly estimated the ages ($t_{\rm gyro}(P_0)$) of solar-type stars with $T_{\rm eff} \sim 5800$ and 5350 K ($B - V \sim 0.65$ and 0.80 from Equation (2) of Valenti & Fischer (2005)) and $P_{\rm rot} \sim 5$, 10, and 20 days. Using these $t_{\rm gyro}(P_0)$ values and Equation (5), we also estimated the fraction of stars as listed in Table 3. We assume that $N_{\rm star}(P_{\rm rot} \geqslant 20 \text{ days})$ is the same as $N_{\rm star}(P_{\rm rot} = 20$–40 days) when we compare it with $N_P(P_{\rm rot} = 20$–40 days) in Table 3. This is because, according to the gyrochronology relation, the rotation period of solar-type stars cannot be larger than 40 days in the duration of the MS phase, and the relation has a breakdown in older, slowly rotating solar-type stars (e.g., $t > 5.0$ Gyr; van Saders et al. 2016; Metcalfe & Egeland 2019).

As seen from Table 3, there are differences between the number fractions of slowly/rapidly rotating stars in the Kepler sample from McQuillan et al. (2014; N_P) and those estimated from the gyrochronology relation ($N_{\rm star}$). In the case of Sun-like stars with $T_{\rm eff} = 5600$–6000 K, the fraction of stars with $P_{\rm rot} = 20$–40 days among all sample stars has roughly a factor of 2 difference: $N_P(P_{\rm rot} = 20$–40 days)$/N_{P,\rm all} \sim 32\%$ and $N_{\rm star,all}(P_{\rm rot} = 20$–40 days)$/N_{\rm star,all} \sim 70\%$. This means that
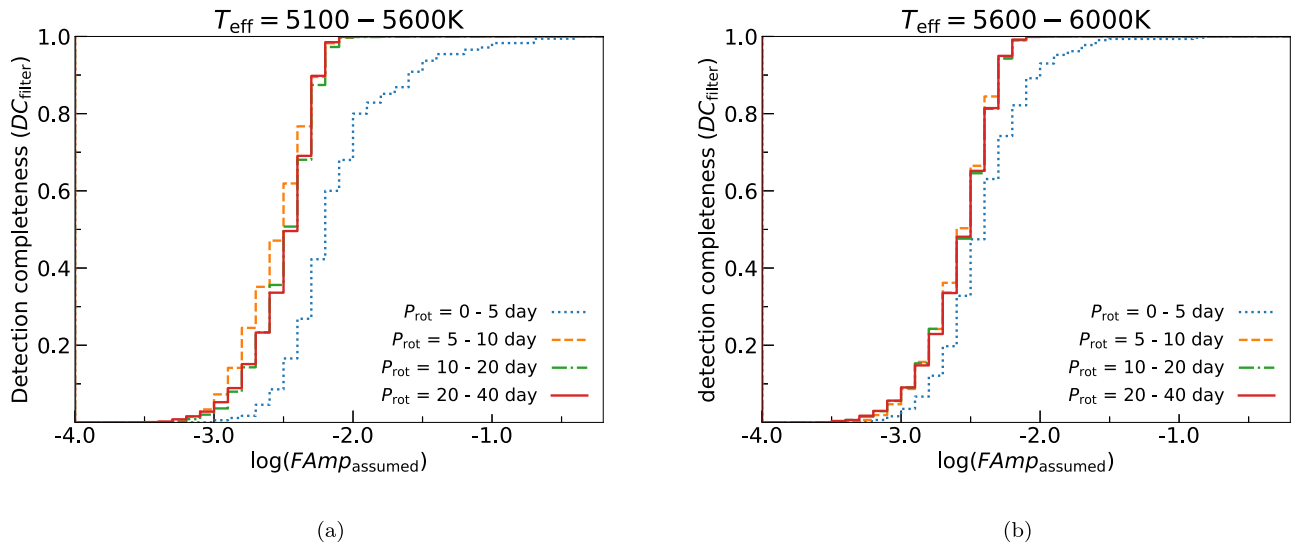
Figure 7. Relationship between DC_{filter} and the assumed flare amplitude (FAmp$_{assumed}$) for several P_{rot} ranges, estimated from the filtered light-curve data (see Figures 1(c) and (d)) of the solar-type stars with the brightness variation period and amplitude (P_{rot} and Amp) values detected in McQuillan et al. (2014; see N_P values in Table 3). The horizontal axis is the logarithm of the assumed amplitude of the flares (FAmp$_{assumed}$). The data are divided into panels (a) and (b) on the basis of stellar temperature: (a) T_{eff} = 5100–5600 K and (b) T_{eff} = 5600–6000 K. Different lines correspond to P_{rot} ranges: blue dotted lines are the values of P_{rot} = 0–5 days, orange dashed lines are those of P_{rot} = 5–10 days, green dashed–dotted lines are those of P_{rot} = 5–10 days, and red solid lines are those of P_{rot} = 20–40 days.

the flare frequency value of Sun-like stars (T_{eff} = 5600–6000 K and P_{rot} > 20 days) can become a factor of 2 smaller than the real value if we only consider the Sun-like stars in McQuillan et al. (2014). We have already shown these differences in Appendix B of Notsu et al. (2019) only as a caution. In this study, we consider the differences when discussing flare frequencies in the following sections. Through this, we aim to discuss more accurate values of flare frequencies, especially for slowly rotating Sun-like stars.

Before applying these "gyrochronology corrections" to flare frequency discussions in the following section, we note several possible errors that the gyrochronology can have. One example is that the age–rotation relation (gyrochronology relation) of young ($t \lesssim$ 0.5–0.6 Gyr) and old ($t \gtrsim$ 5.0 Gyr) solar-type stars can have a large scatter (e.g., Soderblom et al. 1993; Ayres 1997; Tu et al. 2015) and breakdown (van Saders et al. 2016; Metcalfe & Egeland 2019), respectively, as mentioned in Section 3.2. We also assumed that the star formation rate around the Kepler field has been roughly constant over τ_{MS} in the above estimation, but this assumption is not necessarily correct. We should keep these potential errors in mind.

3.6. Flare Detection Limit

As shown in our previous study, Shibayama et al. (2013), the threshold to detect superflares used in our method (see Section 2.1) tended to be larger in rapidly rotating stars than in slowly rotating stars. We used the high-pass filter described in Section 2.1 to eliminate this tendency. In this section, we evaluate how this tendency is changed by the filter and how much this tendency remains in the filtered data to discuss the relations between rotation period and flare frequency in the following sections. As described in Section 2.1, a flare is detected if the assumed flare amplitude (FAmp$_{assumed}$) is larger than the flare detection threshold (*Threshold*). The *Threshold* value is calculated as three times the value at the value of the top 1% of the brightness distribution of each star (See Figure 1). Here we check how large-amplitude flares can be detected (FAmp$_{assumed} \geqslant$ *Threshold*) for each star. We count

the number of stars that satisfy FAmp$_{assumed} \geqslant$ *Threshold* for several period ranges (P_{rot} = 0–5, 5–10, 10–20, and 20–40 days) as a function of FAmp$_{assumed}$: $N_P^{FAmp_{assumed} \geqslant Threshold}$. Then we can define the detection completeness (DC_{filter}) as

$$DC_{filter} = \frac{N_P^{FAmp_{assumed} \geqslant Threshold}}{N_P}, \tag{6}$$

where N_P is the total number of solar-type stars having P_{rot} values in the considered P_{rot} and temperature range shown in Table 3. Here DC_{filter} means the fraction of stars from which flares can be surely detected, since the flare amplitude is larger than the detection threshold (FAmp$_{assumed} \geqslant$ *Threshold*).

Figure 7 shows the relationship between DC_{filter} and the flare amplitude for several period ranges (P_{rot} = 0–5, 5–10, 10–20, and 20–40 days) for the filtered light-curve data (see Figures 1(c) and (d)). There is a tendency for the detection completeness DC_{filter} to become larger as the flare amplitude becomes larger. However, the tendencies are different between rapidly rotating (P_{rot} < 5 days) and slowly rotating ($P_{rot} \geqslant$ 5 days) stars. As for the stars with $P_{rot} \geqslant$ 5 days, the detection completeness DC_{filter} becomes almost ~1.0 at the flare amplitude of ~10^{-2}. This means that we can detect almost all of the superflares on the stars with $P_{rot} \geqslant$ 5 days, if the flare amplitudes are $\geqslant 10^{-2}$. We note that this flare amplitude value of 10^{-2} corresponds to the flare energy with $10^{34.5}$ erg in the case of typical duration superflares in our sample. In contrast, for the rapidly rotating stars with P_{rot} < 5 days, the detection completeness DC_{filter} is still ~0.7 at a flare amplitude of ~10^{-2}. This means that we miss 30% of superflares with an amplitude value of 10^{-2} occurring on stars with P_{rot} < 5 days, while we can detect 70% of superflares with an amplitude value of 10^{-2} occurring on stars with P_{rot} < 5 days.

This difference means that it is difficult to detect smaller superflares on rapidly rotating stars and corresponds to the apparent negative correlation between the rotation period and the lower limit of the flare energy seen in Figure 3. This difference also can be explained by how rapidly rotating stars
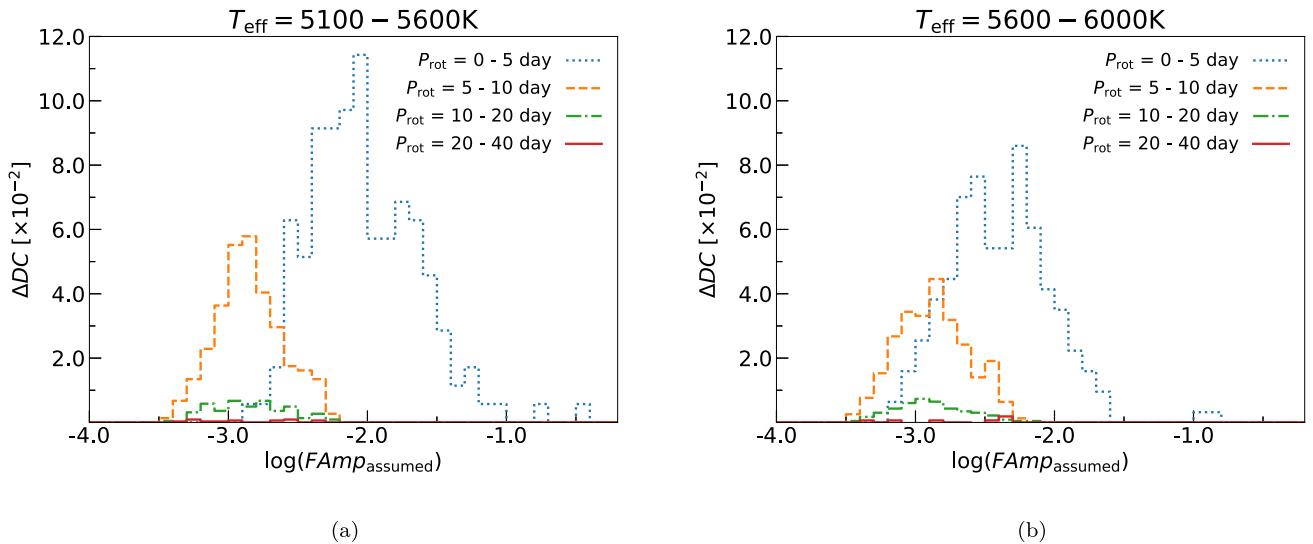
Figure 8. Histograms showing how much the high-pass filter has improved the detection completeness (DC). The vertical axis (ΔDC) is the difference between the detection completeness from the high-pass filtered data (DC_{filter}) and without a high-pass filter (DC_{original}). The data are divided into panels (a) and (b) on the basis of the stellar temperature: (a) $T_{\text{eff}} = 5100$–5600 K and (b) $T_{\text{eff}} = 5600$–6000 K.

tend to have a larger amplitude of the brightness variations (e.g., Figure 6) and the threshold values for the flare detection can be larger. In addition to Figure 7, using the filtered light-curve data, we also calculated DC_{filter} values for the original light-curve data without the high-pass filter process (see Figures 1(a) and (b)), DC_{original}. Then ΔDC is defined as the difference between the detection completeness from the high-pass filtered data (DC_{filter}) and without a high-pass filter (DC_{original}). As shown in Figure 8, the high-pass filter has caused the detection completeness to be improved by a few percent, especially for the rapidly rotating stars ($P < 5$ days), though large effects of the brightness variations remain, as already seen in Figure 7.

We take into account these dependences of the detection completeness (or "missing rate of flares") on the rotation period and flare amplitude when we discuss the relationship between the rotation period and superflare frequency in Section 3.7.

3.7. Frequency Distribution of Superflares and the Dependence on the Rotation Period

We then discuss the flare frequency distributions and their relation to rotation period by using the updated sample of superflares from the Kepler 4 yr data (quarters 0–17) in this study. Figures 9 and 10 represent the occurrence frequency distributions of superflares on solar-type stars with $T_{\text{eff}} = 5600$–6000 and 5600–6000 K, respectively, for the P_{rot} ranges of <5, 5–10, 10–20, and 20–40 days. These occurrence rate values of superflares are estimated for each P_{rot} bin from the number of observed superflares and stars and the total length of the observational period. The potential effects of the gyrochronology correction (Section 3.5) and the flare detection completeness correction (Section 3.6) are not taken into consideration in Figures 9(a) and 10(a). These are the same definitions of flare frequencies as in our previous studies (e.g., Shibayama et al. 2013; Notsu et al. 2019). In Figures 9(b) and 10(b), the frequency values are calculated by incorporating the effect of the gyrochronology correction (Section 3.5) and the flare detection completeness correction (Section 3.6). In order to calculate the frequency of superflares incorporating the effect of gyrochronology correction, we used

N_{star} instead of N_P in Table 3 as a value of the number of observed stars in each P_{rot} bin. Through this, we aim to discuss more accurate values of flare frequencies, especially for slowly rotating Sun-like stars. In order to calculate the frequency of superflares incorporating the effect of the flare detection completeness correction, we correct the number of superflares in each energy and P_{rot} bin by using the relationship among DC_{filter} (detection completeness), flare amplitude, and P_{rot} shown in Figure 7. From the value of DC_{filter} in Figure 7, we can estimate how many flares are missed for each P_{rot} and E_{flare} (flare energy) range. When we estimate the flare frequency, we correct the number of superflares in each P_{rot} and E_{flare} by replacing the number of flares with "(the number of flares)$/DC_{\text{filter}}$." In this process, we assume the average relationship among flare amplitude, flare duration, and E_{flare} for solar-type stars (see energy versus duration, discussed in Maehara et al. 2015). It is assumed that the first data point is the flare with the same value as the threshold, the second point is half of the threshold, and the flare does not continue longer than 1 hr. This does not include various flares, such as long or small flares or superflares with sharp declines.

We also estimate the potential errors of superflare frequency. The number of superflares found in the study is followed by the Poisson statistics, and the estimated σ is $\sqrt{N_{\text{flare}} + 1}$, where N_{flare} is the number of flares in each P_{rot} bin. We include these errors in Figures 9(a) and 10(a). Additionally, we include the following errors in Figures 9(b) and 10(b). The error from the sensitivity correction is from the number of stars that satisfies $\text{FAmp}_{\text{assumed}} \geqslant Threshold$ ($N_P^{F\text{Amp}_{\text{assumed}} \geqslant Threshold}$). We estimate that σ is $\sqrt{N_P^{F\text{Amp}_{\text{assumed}} \geqslant Threshold}}$. The gyrochronology relation error is from the error values of Equations (12)–(14) of Mamajek & Hillenbrand (2008).

Comparing the results without and with corrections in Figures 9 and 10 shows two clear changes. First, because of the sensitivity correction, the smaller-amplitude events—which were originally missed, as shown in Figure 7—are now included in the calculation of the flare frequency, and the frequency value in the smaller-energy superflares ($\lesssim 10^{34}$ erg) becomes larger. The difference is larger, especially for rapidly rotating stars ($P_{\text{rot}} < 5$ days), since the detection completeness
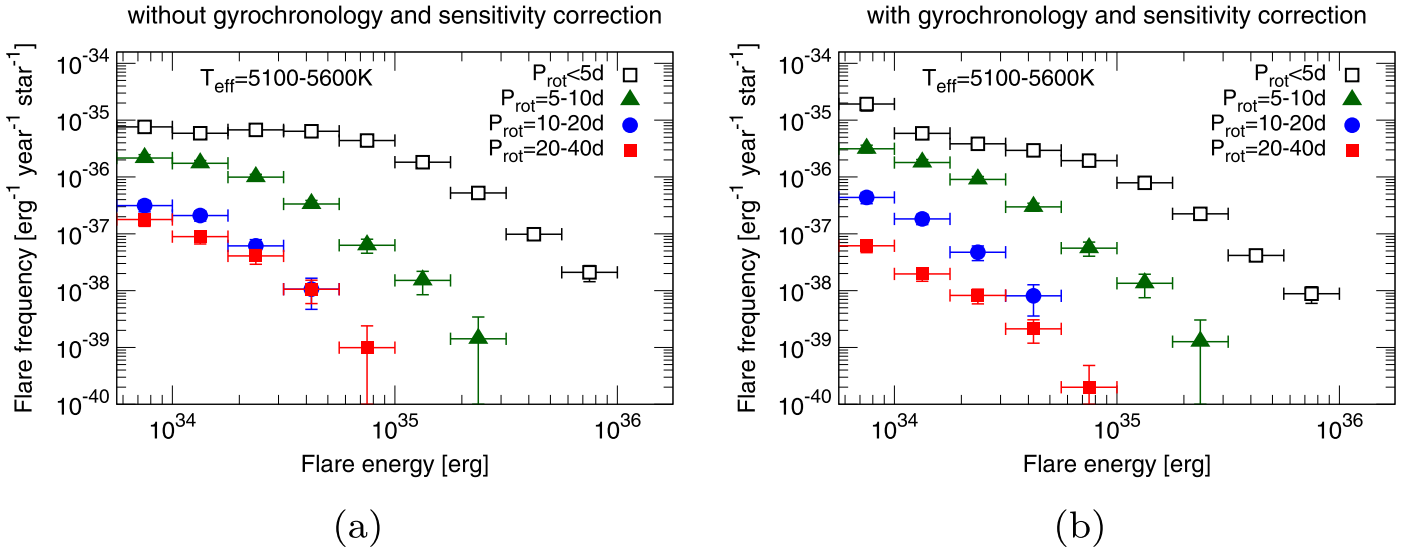
Figure 9. Occurrence frequency distribution of superflares on solar-type stars with $T_{eff} = 5100$–5600 K using the superflare data that are found from Kepler 30 minute cadence data of 4 yr (Q0-17). The horizontal axis is the flare energy, and the error bar in the horizontal axis indicates each energy bin. The vertical axis indicates the number of superflares per star, year, and unit energy in each energy bin. The error bars in the vertical axis are explained in the main text. The symbols are classified with rotation period (P_{rot}) values: black open squares for $P_{rot} < 5$ days, green triangles for $P_{rot} = 5$–10 days, blue circles for $P_{rot} = 10$–20 days, and red filled squares for $P_{rot} = 20$–40 days. The potential errors from the gyrochronology and flare detection completeness are not taken into consideration in panel (a), while in panel (b), the frequency values are calculated by taking into consideration the effect of gyrochronology and flare detection completeness.
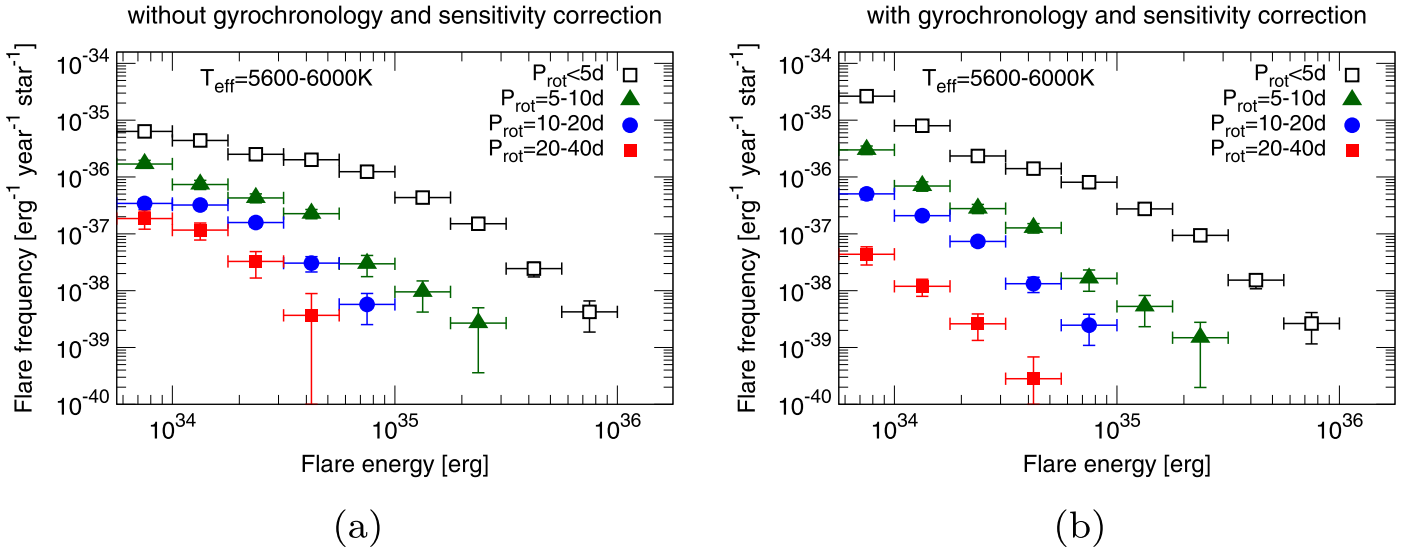
Figure 10. Same as Figure 9, but for $T_{eff} = 5600$–6000 K.

of rapidly rotating stars is smaller than that of slowly rotating stars, as shown in Figure 7. For example, the frequency value of flares with $10^{33.75}$–$10^{34.0}$ erg on stars with $T_{eff} = 5600$–6000 K and $P_{rot} < 5$ days in Figure 10(a) (without correction) is $< 10^{-35}$ erg^{-1} yr^{-1} star^{-1}, but that in Figure 10(b) (with correction) is $> 10^{-35}$ erg^{-1} yr^{-1} star^{-1}. Second, because of the gyrochronology correction (using N_{star} instead of N_P in Table 3 as a value of the number of observed stars in each P_{rot} bin), the exact values of the flare frequencies change, while the shape of the overall distributions (e.g., the power-law distributions in the following) is not affected by this correction. For example, the frequency of slowly rotating Sun-like stars ($T_{eff} = 5600$–6000 K and $P_{rot} = 20$–40 days) becomes about half because of the gyrochronology correction: $N_P(P_{rot} = 20$–40 days$)/N_{P,all} \sim 32\%$ and $N_{star,all}(P_{rot} = 20$–40 days$)/N_{star,all} \sim 70\%$ in Table 3.

As our previous studies (e.g., Shibayama et al. 2013; Notsu et al. 2019) presented, these distributions can be described by a power law ($dN/dE \propto E^{\alpha}$), and rapidly rotating stars tend to have larger frequency values. The power-law indexes (α) of the distributions in Figures 9(b) and 10(b) are listed in Table 4. We estimated the power-law relation ($dN/dE \propto E^{\alpha}$) using all points from the P_{rot} bins shown in the figures, and the error is shown as the vertical error bars.

The indexes are roughly around $\alpha \sim -2$, which can be consistent with previous studies of superflares on solar-type stars (e.g., Shibata et al. 2013; Shibayama et al. 2013; Maehara et al. 2015; Notsu et al. 2019; Tu et al. 2020). We should note that the sensitivity correction in this study (see Figure 7) is a very simple one, only discussing the flare amplitude, and can be an incomplete correction, as we described above. Because of this, the power-law distributions in the smaller energy region
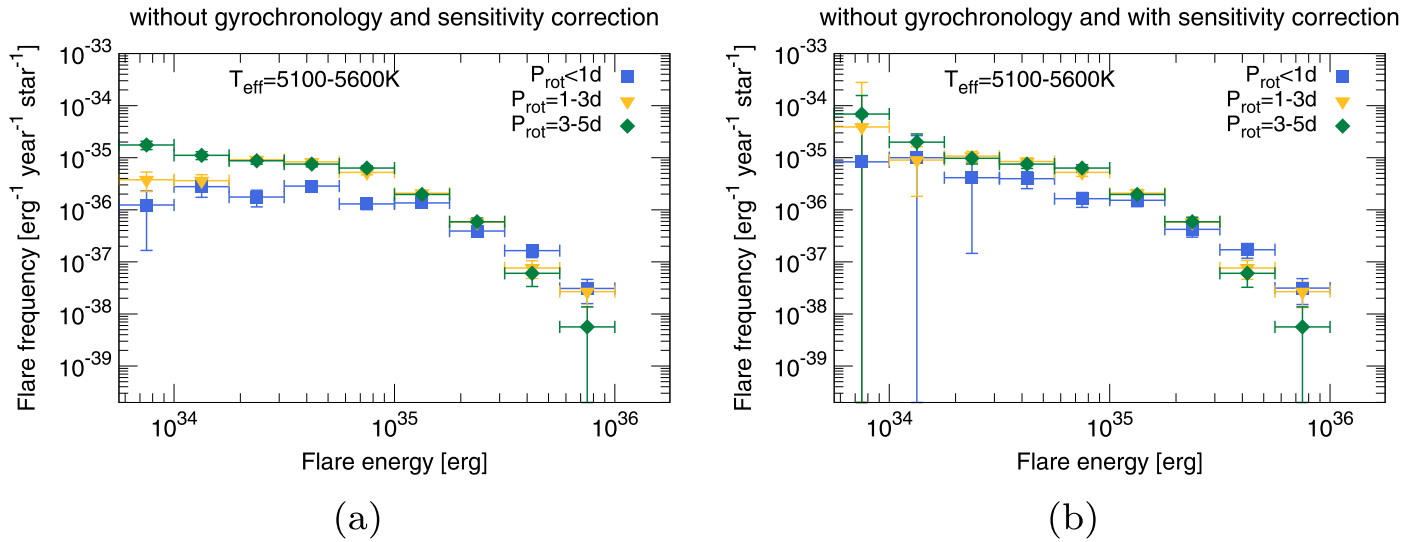
Figure 11. Occurrence frequency distribution of superflares on solar-type stars with $T_{\rm eff}$ = 5100–5600 K and short rotation periods ($P_{\rm rot}$ < 5 days). The symbols are classified with rotation period ($P_{\rm rot}$) values: blue squares for $P_{\rm rot}$ < 1 day, orange triangles for $P_{\rm rot}$ = 1–3 days, and green diamonds for $P_{\rm rot}$ = 3–5 days. The horizontal axes, vertical axes, and definitions of error bars are the same as in Figure 9, while we note that the range of the vertical axes is a bit different from Figure 9. The potential errors from the gyrochronology and flare detection completeness are not taken into consideration in panel (a), while in panel (b), the frequency values are calculated by taking into consideration the effect of the flare detection completeness. Different from Figure 9(b), the gyrochronology effect is not considered in panel (b) of this figure, since the age–rotation relation (gyrochronology relation) of young solar-type stars can have a large scatter (e.g., Soderblom et al. 1993; Ayres 1997; Tu et al. 2015), as mentioned in Section 3.2.

Table 4
Power-law Index ($dE/dN \propto E^{\alpha}$) of Flare Frequency Distributions in Each Rotation Bin

	$T_{\rm eff}$ = 5100–5600 K	$T_{\rm eff}$ = 5600–6000 K
$P_{\rm rot}$ < 5 days	−1.5 ± 0.1 (−2.9 ± 0.1)	−1.8 ± 0.1 (−3.1 ± 0.1)
$P_{\rm rot}$ = 5–10 days	−1.9 ± 0.2 (−2.9 ± 0.4)	−2.1 ± 0.1 (−2.1 ± 0.1)
$P_{\rm rot}$ = 10–20 days	−2.2 ± 0.2 (−2.6 ± 0.2)	−2.2 ± 0.1 (−3.0 ± 0.1)
$P_{\rm rot}$ = 20–40 days	−2.1 ± 0.2 (−2.9 ± 0.5)	−2.7 ± 0.1 (−3.0 ± 0.3)

Note. We calculate the power-law index from Figures 9(b) and 10(b). The power-law index without parentheses is calculated from all points in each $P_{\rm rot}$ bin, while the numbers within parentheses show the power-law index using three larger flare energy points in each $P_{\rm rot}$ bin.

($\lesssim 10^{34}$ erg) can have some systematic errors that are not included in the error bars in Figures 9(b) and 10(b). We should keep this in mind when we see the power-law indexes listed in Table 4.

The upper-limit values of flare energy roughly depend on rotation period, as already seen in Figure 3. As also seen in the index values listed in Table 4, we can see that the power-law distribution becomes a bit steeper as the flare energy becomes larger. For example, the power-law index of superflares on Sun-like stars ($T_{\rm eff}$ = 5600–6000 K and $P_{\rm rot}$ = 20–40 days) in Figure 10(b) is $\alpha \sim -2.7$ if we calculate using the data of $10^{33.75}$ erg < $E_{\rm flare}$ < $10^{34.75}$ erg. However, if we use the data of $10^{34.0}$ erg < $E_{\rm flare}$ < $10^{34.75}$ erg, the power-law index α is ~ -3.0. Similar tendencies can also be seen for the stars with $P_{\rm rot}$ < 20 days in Table 4, while we should note that the number of larger-energy flares is small, and the exact values of α should be treated with great caution. These tendencies might be related to the maximum flare energy cutoff of solar-type stars, since there is a correlation between the maximum spot coverage and the rotation period (Figure 6), and the spot size can explain the flare energy (Figure 4). In the case of old (age $\sim$ 4.6 Gyr), slowly rotating Sun-like stars with $T_{\rm eff}$ = 5600–6000 K and

$P_{\rm rot} \sim 25$ days, as also described in Section 3.4, Figure 6(b) shows that the maximum size of the starspots is a few percent of the solar hemisphere. This corresponds to 10^{34}–10^{35} erg on the basis of Equation (4), and the upper limit of the superflare energy of these Sun-like stars in Figures 3 and 10(b) is roughly in the same range.

Next, for reference, we see the flare frequency distributions of rapidly rotating stars with $P_{\rm rot}$ < 5 days in a bit more detail. Like Figures 9 and 10, Figures 11(a) and 12(a) are the flare frequency distributions of $P_{\rm rot}$ < 1, 1–3, and 3–5 days without the gyrochronology and sensitivity corrections, and Figures 11(b) and 12(b) are those with only the sensitivity correction. Since the gyrochronology relation has a larger scatter at a younger age ($\lesssim$ 0.5–0.6 Gyr), as described in Section 3.2, the gyrochronology correction is not included in Figures 11(b) and 12(b). Although the original sample size of rapidly rotating stars is small (see N_P values in Table 3), we can still see the power-law distributions for very rapidly rotating stars in the range of $E_{\rm flare} \gtrsim 10^{34.5}$ erg (e.g., $P_{\rm rot}$ < 1 day).

We then see the relation between flare frequency and rotation period by using the superflare data that include the above gyrochronology and sensitivity corrections. Figure 13 shows that the average flare frequency in a given period bin tends to decrease as the period increases in the range of $P_{\rm rot}$ longer than a few days, as we have already seen the same tendency in Figures 9(b) and 10(b). This result is basically the same as that presented in our previous study (Notsu et al. 2019), but the sample size is much larger, especially for slowly rotating stars (see Section 3.1). The frequency of superflares on young, rapidly rotating stars ($P_{\rm rot}$ = 1–3 days) is $\sim$100 times higher compared with old, slowly rotating stars ($P_{\rm rot}$ > 20 days), and this indicates that as a star evolves (and its rotational period increases), the frequency of superflares decreases. In contrast, the flare frequency is roughly constant in the range of $P_{\rm rot} \lesssim$ 3 days. We note that in this range of $P_{\rm rot} \lesssim$ 3 days, flare frequency distributions still show similar power-law distributions (Figures 11(b) and 12(b)). We can now interpret that this
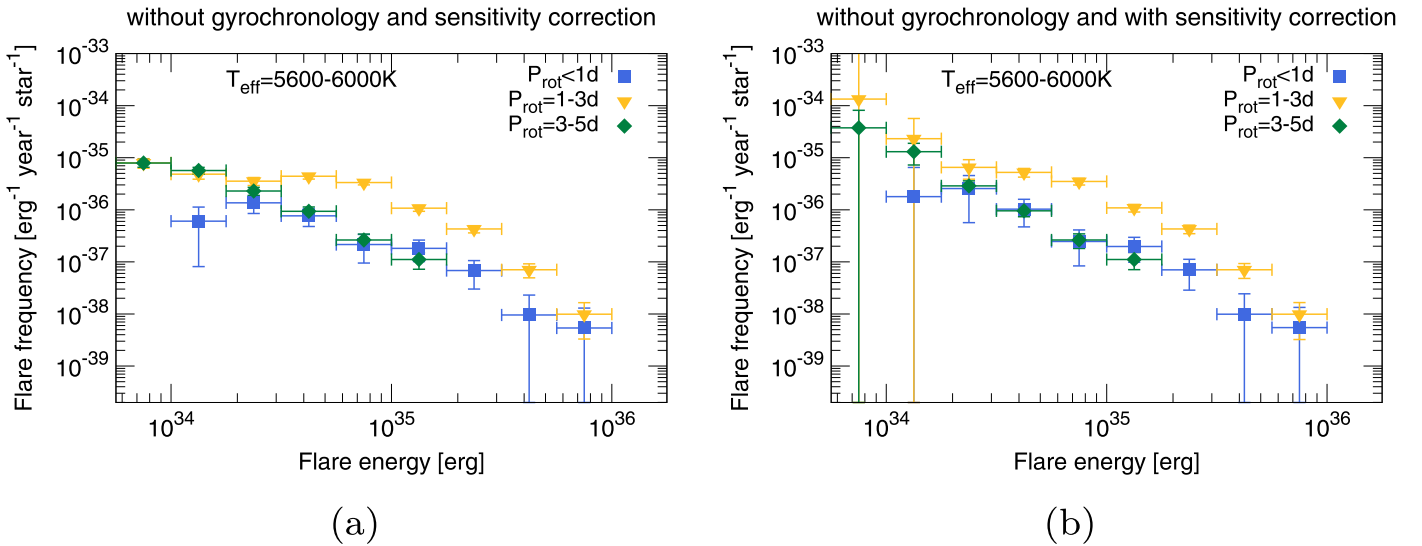
without gyrochronology and sensitivity correction (a)

without gyrochronology and with sensitivity correction (b)

Figure 12. Same as Figure 11, but for the stars with $T_{\rm eff} = 5600–6000$ K.
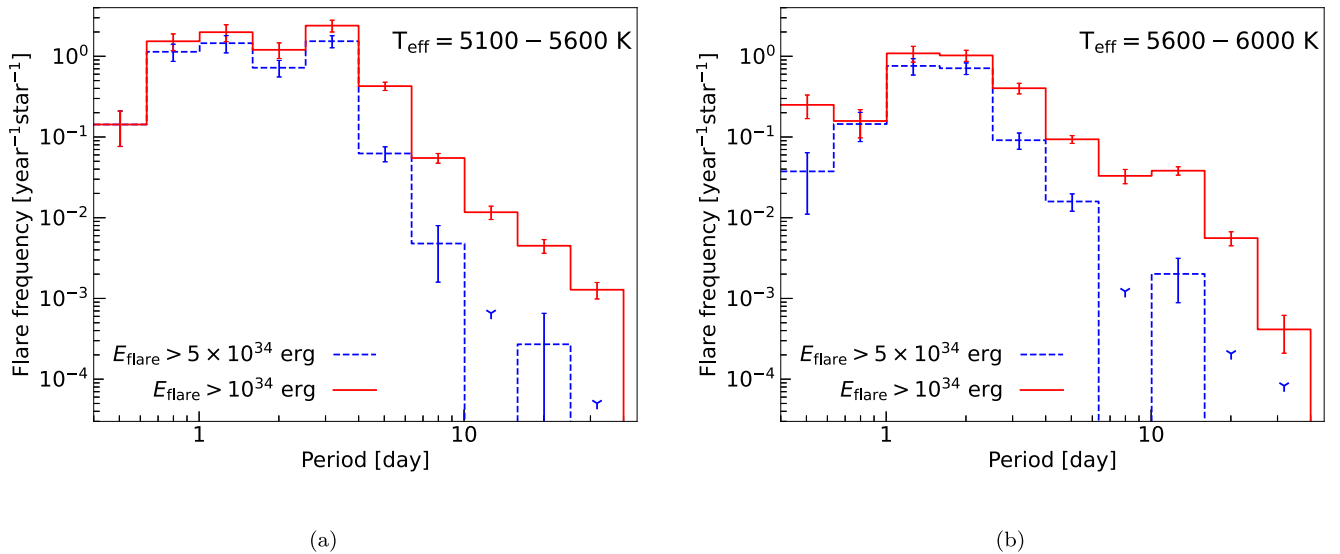

(a)

(b)

Figure 13. Occurrence frequency distributions of superflares as a function of the rotation period ($P_{\rm rot}$) using the superflare data that are found from Kepler 30 minute cadence data of 4 yr (Q0-17). The figures are separated into two temperature ranges: (a) $T_{\rm eff} = 5100–5600$ K and (b) $T_{\rm eff} = 5600–6000$ K. The vertical axes indicate the number of superflares with energy $>5 \times 10^{34}$ erg (blue dashed lines) and $>10^{34}$ erg (red solid lines) per star and year. Error bars in the vertical axis represent the 1σ uncertainty of the frequency, which is estimated in the same way as in Figures 9 and 10. In the long period range ($P_{\rm rot} \gtrsim 5$ days), the frequency values are calculated by taking into consideration the effect of gyrochronology and flare detection completeness, as in Figures 9(b) and 10(b). In the short period range ($P_{\rm rot} < 5$ days), only the flare detection completeness is considered, as in Figures 11(b) and 12(b). As for the blue dashed lines, in the case of no events in a period bin, the upper-limit values are shown with the blue Y-shaped points, assuming that less than one event occurs in each bin.

correlation between the rotation period (roughly corresponding to age) and flare frequency is consistent with the correlation between the rotation period (age) and the quiescent stellar activity level, such as the average X-ray luminosity (e.g., Noyes et al. 1984; Güdel 2007; Wright et al. 2011). The correlation between the rotation period and the X-ray luminosity of solar-type stars also shows a "saturation" regime in the range of $P_{\rm rot} \lesssim 3$ days and a "decreasing trend" in the range of $P_{\rm rot} \gtrsim 3$ days.

3.8. Superflare Frequency on Sun-like Stars and Implications for the Sun

Our previous study (Shibayama et al. 2013; Maehara et al. 2015; Notsu et al. 2019) pointed out that the frequency distribution of superflares on Sun-like stars is roughly on the same power-law line. However, the definition of Sun-like stars in Shibayama et al. (2013) and Maehara et al. (2015; $T_{\rm eff} = 5600–6000$ K and $P_{\rm rot} > 10$ days) is different from that of this study ($T_{\rm eff} = 5600–6000$ K and $P_{\rm rot} = 20–40$ days). This indicates that many younger stars are included (e.g., stars with $P_{\rm rot} \sim 10$ days have an age of $t \sim 1$ Gyr). Notsu et al. (2019) used the same definition of Sun-like stars as this study in order to discuss only the data of stars rotating as slowly as the Sun ($P_{\rm rot} \sim 25$ days and $t \sim 4.6$ Gyr). However, as also described in this paper, the sample size of Notsu et al. (2019) was so small that we were not able to discuss the detailed properties accurately. Moreover, different from this study, our previous studies (Shibayama et al. 2013; Maehara et al. 2015;
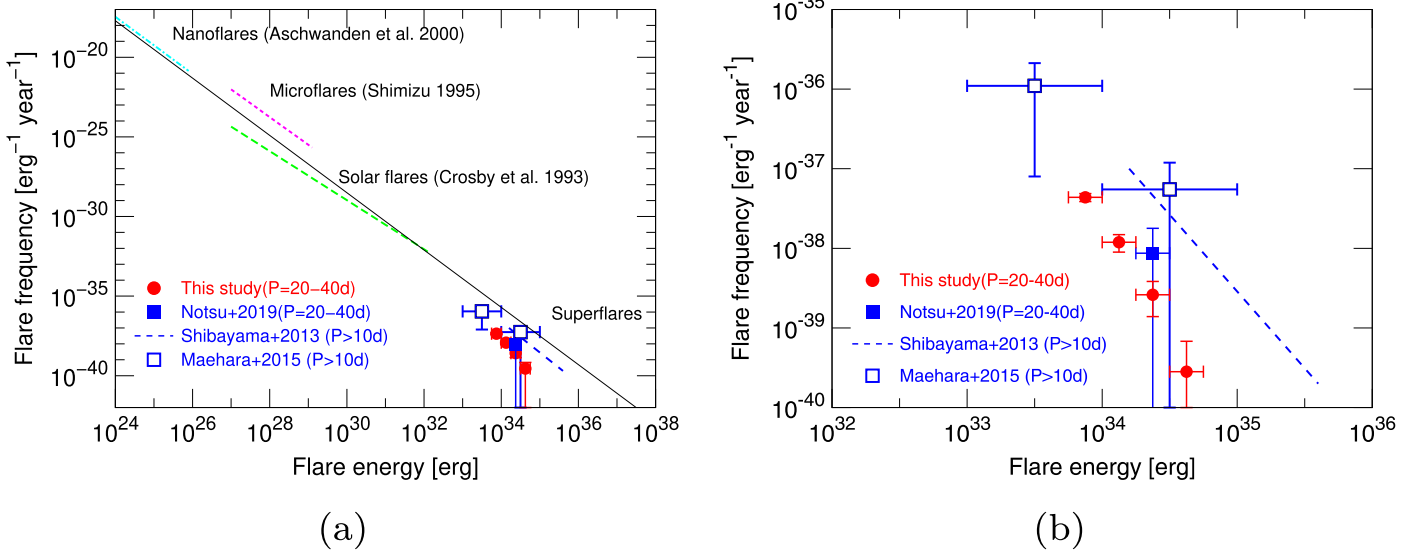
Figure 14. (a) Comparison between the frequency distribution of superflares on Sun-like stars and solar flares. The red filled circles, blue filled squares, blue dashed lines, and blue open squares indicate the occurrence frequency distributions of superflares on Sun-like stars (slowly rotating solar-type stars with $T_{\rm eff} = 5600$–6000 K). The red filled circles correspond to the updated frequency values of superflares on Sun-like stars with $P_{\rm rot} = 20$–40 days, which are calculated with gyrochronology and sensitivity correction in this study and presented in Figure 10(b). Horizontal and vertical error bars are the same as those in Figure 10(b). For reference, the blue filled squares are the values of Sun-like stars with $P_{\rm rot} = 20$–40 days, which we presented in Figure 17 of Notsu et al. (2019). Also for reference, the blue dashed lines and blue open squares are the values of the superflares on the stars with $P_{\rm rot} > 10$ days, which we presented in Figure 4 of Maehara et al. (2015) on the basis of original superflare data using Kepler 30 (Shibayama et al. 2013) and 1 (Maehara et al. 2015) minute cadence data, respectively. Three dashed lines on the upper left side of this figure indicate the power-law frequency distribution of solar flares observed in the hard X-ray (Crosby et al. 1993), soft X-ray (Shimizu 1995), and extreme UV (Aschwanden et al. 2000). Occurrence frequency distributions of superflares on Sun-like stars and solar flares are roughly on the same power-law line with an index of -1.8 (black solid line) for the wide energy range between 10^{24} and 10^{35} erg. (b) Same as panel (a), but only the data of the superflares are plotted.

Notsu et al. 2019) did not include the effect of gyrochronology and flare detection completeness (sensitivity) correction when discussing the flare frequency distribution. Then, in Figure 14, we newly plot the frequency value of superflares on Sun-like stars with $P_{\rm rot} = 20$–40 days ($t > 3.2$ Gyr) taken from Figure 10(b), in addition to the data of solar flares and superflares shown in Figure 17 of Notsu et al. (2019).

The newly added data points of the superflares on Sun-like stars are roughly on the same power-law line. The exact value of the superflare frequency with $P_{\rm rot} = 20$–40 days in this study is a bit smaller than that of Notsu et al. (2019), as clearly seen in Figure 14(b), mainly because the gyrochronology correction is newly included in this study. As also mentioned in Section 3.7, it might be possible that the frequency distribution of superflares becomes steeper around the upper limit of the superflare energy ($E_{\rm flare} \sim 5 \times 10^{34}$ erg), but we cannot judge whether this possibility is true in the case of superflares on Sun-like stars because of the limited number of superflares detected on Sun-like stars in this study (see Table 2). We also note that some of the Sun-like superflare stars plotted in Figure 14 have flag 1 in Table 2. This means it is difficult to finally judge whether these stars really have rotation periods as slow as the Sun ($P_{\rm rot} = 20$–40 days), and we need to be cautious (see Appendix A) when discussing the frequency of superflares on Sun-like stars in Figure 14. More investigations including spectroscopic measurements of rotation periods for all of these slowly rotating Sun-like superflare stars (e.g., Notsu et al. 2015b, 2019) are needed in the future.

As a result of Figure 14, we can roughly remark that superflares with energy $E_{\rm flare} \sim 10^{33.75}$, $\sim 10^{34.0}$, $\sim 10^{34.25}$, and $\sim 10^{34.5}$ erg would be approximately once every ~ 3000, ~ 6000, $\sim 16{,}000$, and $\sim 85{,}000$ yr on old, slowly rotating Sun-like stars with $P_{\rm rot} \sim 25$ days and $t \sim 4.6$ Gyr. These results of the superflare

frequency distribution of Sun-like superflare stars (e.g., Figure 14) have shown the possibility that superflares whose energy is $\sim 7 \times 10^{33}$ erg ($\sim$X700-class flares; see Figure 4) can occur on our Sun once every ~ 3000 yr, those with $\sim 1 \times 10^{34}$ erg ($\sim$X1000-class flares; see Figure 4) once every ~ 6000 yr, and those larger than 1×10^{34} erg can occur with longer timescales (e.g., once every $\gtrsim 10{,}000$ yr). This possibility of superflares on our Sun is now supported more strongly in this study because of a much larger number of superflares on slowly rotating Sun-like stars compared with our previous studies.

In contrast, the possibility of superflares with energy $> 10^{34}$ erg has been questioned by several studies. Aulanier et al. (2013) suggested that it is unlikely that the current solar convective dynamo can produce the giant sunspot groups necessary for such large superflares (see Figure 4), since such giant sunspot groups have not been recorded in solar observations for a few hundred years (see Schrijver et al. 2012). Schmieder (2018) also supported the idea that with our Sun as it is today, it seems impossible to get larger sunspots and superflares with energy $> 10^{34}$ erg. However, in Section 3.4, we have already seen that slowly rotating Sun-like stars ($T_{\rm eff} = 5600$–6000 K, $P_{\rm rot} \sim 25$ days, and $t \sim 4.6$ Gyr) have starspots with a size of $\sim 1\%$ of the solar hemisphere (Figure 6). This spot size value is enough for $\gtrsim 10^{34}$ erg superflares on the basis of Equation (4), and the upper limit of the superflare energy of these Sun-like stars in this study (e.g., Figures 3 and 14) is roughly in the same range. The possible existence of such large starspots on Sun-like stars and the Sun is also suggested in the Kepler data analyses (Maehara et al. 2017; Notsu et al. 2019). Shibata et al. (2013) also suggested that even the current Sun can generate the large magnetic flux necessary for 10^{34} erg superflares in a typical dynamo model.

Moreover, Maehara et al. (2017) and Notsu et al. (2019) also investigated the size–frequency distribution of these large starspot groups on Sun-like stars and that of sunspots and revealed that both sunspots and larger starspots could be related to the same physical processes. In Figure 18 of Notsu et al. (2019), they found that the occurrence frequency decreases as the area of sunspots or starspots increases, and the distribution of sunspot groups for large sunspots is roughly on this power-law line, although the appearance frequency of sunspots with spot areas of ∼1% of the solar hemisphere is about 10 times lower than that of starspots on Sun-like stars. The difference between the Sun and Sun-like stars might be caused by the lack of a "superactive" phase on our Sun during the past 140 yr (Schrijver et al. 2012). The upper limit of the starspot size values of Sun-like stars in Figure 18 of Notsu et al. (2019) is approximately a few percent of the solar hemisphere, and the appearance frequency of these spots is approximately once every 2000–3000 yr. As a result, these results of starspot frequency in Maehara et al. (2017) and Notsu et al. (2019) can be consistent with those of superflare frequency in this section (e.g., Figure 14).

Finally, it is interesting to note that several potential candidates of extreme solar flare events, which can be bigger than the largest solar flare in the past 200 yr ($E_{flare} \sim 10^{32}$ erg), have been reported from the data over the last 1000–2000 yr (e.g., see Usoskin 2017 and Miyake et al. 2019 for reviews). For example, significant radioisotope ^{14}C and ^{10}Be enhancements have been reported in tree rings and ice cores for the years AD 775, AD 994, and BC 660. They suggest extremely strong and rapid cosmic-ray increase events possibly caused by extreme solar flares (e.g., Miyake et al. 2012, 2013; Mekhaldi et al. 2015; O'Hare et al. 2019). These potential high-energy particle events can be caused by the superflares whose energies are at least larger than 10^{33} erg (Cliver et al. 2020), although there is a large scatter between the flare energy and flux of energetic particles on the surface of the Earth (e.g., Takahashi et al. 2016), and more investigations are necessary. Besides, various potential low-latitude auroral and large sunspot drawings have also been reported from historical documents around the world, and they suggest the possibility that extreme solar flare events have occurred several times in the past ∼1000 yr (e.g., Hayakawa et al. 2017b & 2017b). In future studies, the superflare frequency information discussed in this study (e.g., Figure 14) should be compared with these radioisotope and historical data in detail, so that we can discuss the possibility of extreme solar flare events from various points of view.

3.9. Superflare Stars Having Exoplanets

Rubenstein & Schaefer (2000) argued that stars having a hot Jupiter-like companion are good candidates for superflare stars, since the hot Jupiter may play the role of a companion star in binary stars, such as RS CVn stars. The RS CVn stars are magnetically very active and produce many superflares. Since the Sun does not have hot Jupiters, Schaefer et al. (2000) concluded that our Sun has never generated superflares. In order to check the argument, we checked whether the superflare solar-type stars found in this study have any exoplanets, using the data retrieved from the NASA Exoplanet Archive[12] on 2020 May 28. As a result, the solar-type superflare stars found in this study have no confirmed exoplanets, while three

candidate exoplanets[13] and three false-positive exoplanets[14] are found. This suggests that a hot Jupiter is not a necessary condition for superflares on solar-type stars. In addition, Shibata et al. (2013) also found from theoretical considerations that hot Jupiters do not play an essential role in the generation of magnetic flux in the star itself, if we consider only the magnetic interaction between the star and the hot Jupiter, whereas the tidal interaction seems to be a possible cause of enhanced dynamo activity, though more detailed studies will be necessary. This seems to be consistent with the above observational finding that a hot Jupiter is not a necessary condition for superflares on solar-type stars.

4. Conclusion

In our previous studies (Maehara et al. 2012, 2015; & 2017; Shibayama et al. 2013; Notsu et al. 2013b, 2015b; & 2019), we investigated the statistical properties of solar-type and Sun-like superflare stars using the photometric data of the Kepler space telescope. These studies, however, were not enough, since they only had three Sun-like superflare stars, mainly because they only used the first ∼500 days of the Kepler 4 yr primary mission data. Then, in this study, we report the latest statistical analyses of superflares on solar-type (G-type MS) stars using all of the Kepler 4 yr primary mission data covering ∼1500 days and the Gaia-DR2 catalog. Since the catalog was updated to Gaia-DR2, the sample size of solar-type stars became ∼four times larger and the sample size of Sun-like stars became ∼12 times larger than Notsu et al. (2019). We updated the flare detection method by using a high-pass filter to remove rotational variations caused by starspots (Section 2.1). We also took into account the effect of sample biases on the frequency of superflares by considering gyrochronology (Section 3.5) and flare detection completeness (Section 3.6). These results enabled us to discuss a more well-established view of the statistical properties of superflares on Sun-like stars.

(i) We found 2341 superflares on 265 solar-type stars and 26 superflares on 15 Sun-like stars (T_{eff} = 5600–6000 K and P_{rot} = 20–40 days; Table 1). The number of superflares occurring on solar-type stars increased from 527 to 2341, and that of Sun-like stars greatly increased from three to 26 events, compared with Notsu et al. (2019).

(ii) The observed upper limit of the flare energy decreases as the rotation period (stellar age) increases in solar-type stars (Figure 3), while the flare energy can be explained by the magnetic energy stored around starspots (Figure 4). These can be consistent with the result that the starspot coverage decreases as the rotation period increases (Figure 6). In the case of slowly rotating Sun-like stars (T_{eff} = 5600–6000 K, P_{rot} = 20–40 days, and age $t \sim 4.6$ Gyr), superflares with energies up to ∼4×10^{34} erg can occur, while superflares up to ∼10^{36} erg can occur on young, rapidly rotating stars ($P_{rot}\sim$ a few days and $t \sim$ a few hundred Myr). The maximum size of the starspots on old, slowly rotating Sun-like stars and young, rapidly rotating stars is a few percent and ∼10% of the solar hemisphere, respectively, and these correspond to the above upper limits of superflare energies. We notice that the starspot area value estimated from the light curve can be smaller than the value of the real starspot

---

[13] KIC 008946267, KIC 008040308, and KIC 008822421.
[14] KIC 005991070, KIC 008285970, and KIC 012207117.

area (see Section 3.3) and the more energetic flare can occur, since the sample size is limited.

(iii) The frequency of superflares on young, rapidly rotating stars (P_{rot} = 1–3 days) is ∼100 times higher compared with old, slowly rotating stars (P_{rot} > 20 days), and this indicates that as a star evolves (and its rotational period increases), the frequency of superflares decreases (Figure 13). In contrast, the flare frequency is roughly constant in the range of $P_{rot} \lesssim 3$ days.

(iv) The flare frequency distributions of each P_{rot} show the power-law distributions ($dN/dE \propto E^{\alpha}$; Section 3.8). The frequency distributions of superflares on Sun-like stars and of solar flares are roughly on the same power-law line (Figure 14).

(v) From the analysis of Sun-like stars, superflares whose energy is ∼7 × 10^{33} (∼X700-class flares) and ∼1 × 10^{34} (∼X1000-class flares) erg can occur once every ∼3000 and ∼6000 yr, respectively (Figure 14), on the Sun. The results of starspot frequency on Sun-like stars in Notsu et al. (2019) also are consistent with the results of the superflare frequency in this study. These results strongly support the possibility of superflares on the Sun and reveal the frequency of superflares on the Sun through the Sun-like stars.

(vi) The solar-type superflare stars found in this study have no confirmed exoplanets, and this indicates that a hot Jupiter is not a necessary condition for superflares on solar-type stars.

From these results, we have gained great insight into the important question of whether our Sun can have superflares. In future studies, we will clarify the properties of superflare stars on Sun-like stars and get a final conclusion for this question. We have found 15 slowly rotating Sun-like superflare stars in this study, but the number of Sun-like superflare stars (T_{eff} = 5600–6000 K, $P_{rot} \sim 25$ days, and $t \sim 4.6$ Gyr) that have been investigated spectroscopically and confirmed to be "single" Sun-like stars is now zero, as described in Appendix B. Future spectroscopic observations of Sun-like superflare stars are necessary to investigate whether the Sun-like stars really have superflares. Although all of the 15 Kepler Sun-like superflare stars listed in Table 2 are relatively faint (all are fainter than 13.5 mag in Kepler-band magnitude, and most of them are fainter than 14.5 mag), it is very important to conduct spectroscopic observations of these 15 Sun-like Kepler superflare stars in order to confirm the validity of the statistical results of superflares on Sun-like stars discussed in this study using Kepler data (e.g., Figure 14).

In addition, nearby bright superflare stars that are found from TESS (Ricker et al. 2015; Tu et al. 2020; Doyle et al. 2020) and will be found from PLATO (Rauer et al. 2014) can also be good targets for future spectroscopic studies.

The statistical properties of the superflares presented in this study can be combined with many topics to more fully understand the physics of superflares and effects in related research fields, for example, mechanisms of white-light continuum emissions of superflares (e.g., Katsova & Livshits 2015; Namekata et al. 2017; Heinzel & Shibata 2018; Kowalski & Allred 2018; Nizamov 2019); chromospheric line profiles during superflares (e.g., Houdebine et al. 1993; Honda et al. 2018; Namekata et al. 2020b); stellar mass ejections (e.g., coronal mass ejections) during superflares (e.g., Takahashi et al. 2016; Crosley & Osten 2018; Lynch et al. 2019; Moschou et al. 2019; Vida et al. 2019;

Leitzinger et al. 2020); impacts of superflares on planets, especially exoplanets (e.g., Segura et al. 2010; Airapetian et al. 2016, 2020; Atri 2017; Lingam & Loeb 2017; Kay et al. 2019; Linsky 2019; Herbst et al. 2019; Yamashiki et al. 2019); solar activities over ∼1000 yr (e.g., Miyake et al. 2012, 2013, & 2019; Usoskin 2017; Hayakawa et al. 2017b & 2017b); complexities of starspots and starspot distributions of superflare stars (e.g., Maehara et al. 2017; Toriumi & Wang 2019; Doyle et al. 2018; Morris et al. 2018; Roettenbacher & Vida 2018; Takasao et al. 2020); and large starspot lifetimes and formation/decay processes (e.g., Shibata et al. 2013; Giles et al. 2017; Namekata et al. 2019, 2020a; Ikuta et al. 2020). For these points, we plan to conduct long-term spectroscopic monitoring observations of nearby superflare stars using 2–4 m telescopes, especially the Kyoto University Okayama 3.8 m Seimei telescope (Kurita et al. 2020; Namekata et al. 2020b).

Appendix A
Light Curves of All of the Superflares on Sun-like Stars

Since one of the most important points of this paper is investigating whether slowly rotating stars really have superflares, we show the light curves of all of the superflares that occurred on Sun-like stars (all superflares occurred on solar-type stars listed in Table 2). Light curves are separated into Figures 15, 16, and 17, as described in the following. We also show the Lomb–Scargle periodograms of all of the Sun-like superflare stars in order to check whether the P_{rot} values that are taken from McQuillan et al. (2014) and listed in Table 2 are appropriate. Since McQuillan et al. (2014) used a different method (the ACF method; see McQuillan et al. 2014 for details) to estimate rotation period values, these Lomb–Scargle periodograms can be an independent check of P_{rot} values. These periodograms are estimated from all of the available light-curve data of each superflare star. These periodograms are also separated into Figures 18, 19, and 20.

Figures 15 and 18 are the light curves and Lomb–Scargle periodograms of the 10 Sun-like superflare stars that have no
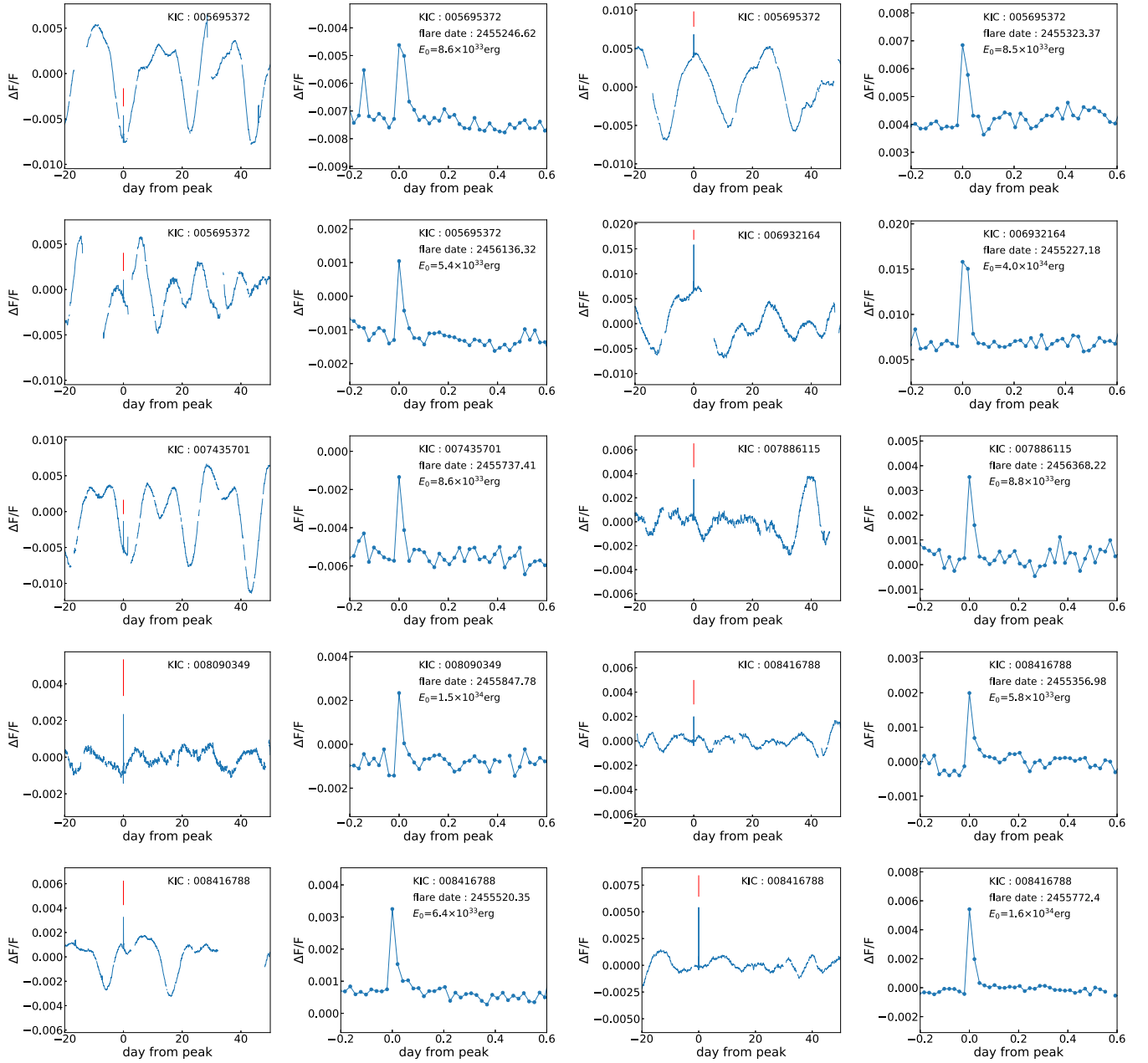
Figure 15. Light curves of all superflares on the 10 Sun-like superflare stars that have no flags in Table 2. Horizontal and vertical axes correspond to days from the flare peak and stellar brightness normalized by the average brightness during the observation quarter of Kepler. As in Figure 2, light curves are provided in pairs of panels. For each pair, the left panel shows the 70 day time variation of stellar brightness to see the periodic brightness variations caused by stellar rotation. The right panel shows the detailed brightness variations of a flare. The star ID (Kepler ID), Barycentric Julian Date of the flare peak, and total released bolometric energy are shown in the right panels.

flags in Table 2. The light curves and Lomb–Scargle period-ograms of these 10 stars look consistent with these stars showing the slow rotation period values ($P_{\rm rot} > 20$ days) taken from McQuillan et al. (2014).

Figures 16 and 19 are the light curves and Lomb–Scargle periodograms of the five Sun-like superflare stars that have flag 1 in Table 2. As shown in Figures 19, these five stars have power peaks in different $P_{\rm rot}$ values from McQuillan et al. (2014), so the real rotation period value of these stars might be different from that used in Table 2. However, the large peaks

are at the half of the rotation period reported by McQuillan et al. (2014). It is quite possible that this does not contradict between the periodograms and McQuillan et al. (2014), because the analysis method used by McQuillan et al. (2014) is resistant to harmonics.

These five stars have flag 1 in Table 2 as a caution, but they are still used in the statistical discussions in the main part of this paper, since it is difficult to finally judge whether the slow rotation period values ($P_{\rm rot} > 20$ days) taken from McQuillan et al. (2014) are correct or not from only the simple light-curve
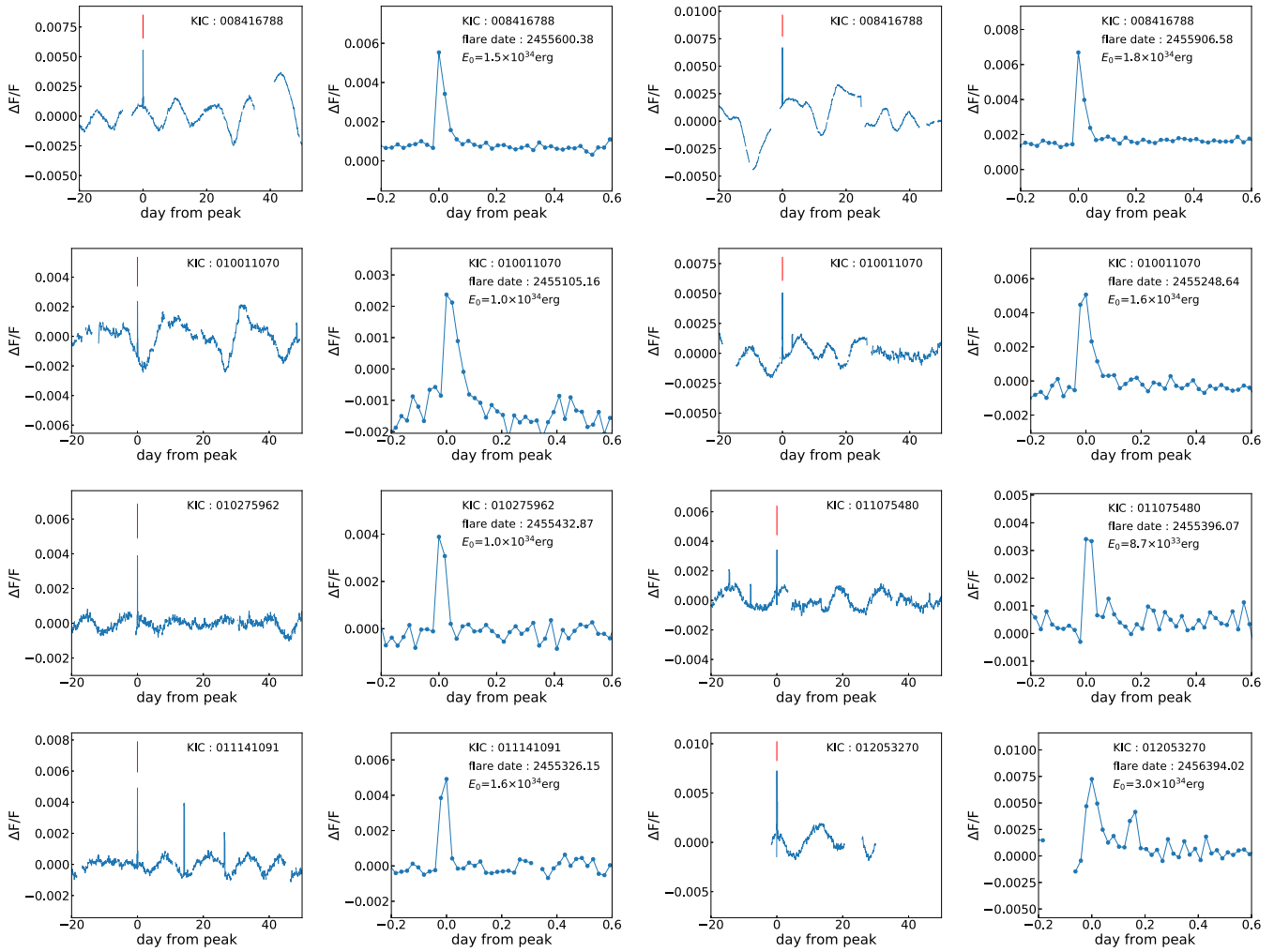
Figure 15. (Continued.)

analyses. More investigations including spectroscopic measurements of rotation periods (e.g., Notsu et al. 2015b, 2019) are needed.

Figures 17 and 20 are the light curves and Lomb–Scargle periodograms of KIC007772296, which has flag 2 in Table 2.

In Figure 17 (left panels), a periodic brightness variation with a period of a few days is found, and also in Figure 20, a sharp peak can be seen around a few days. From these points, we judged KIC007772296 as a binary candidate and eliminated it from statistical analyses in the study.
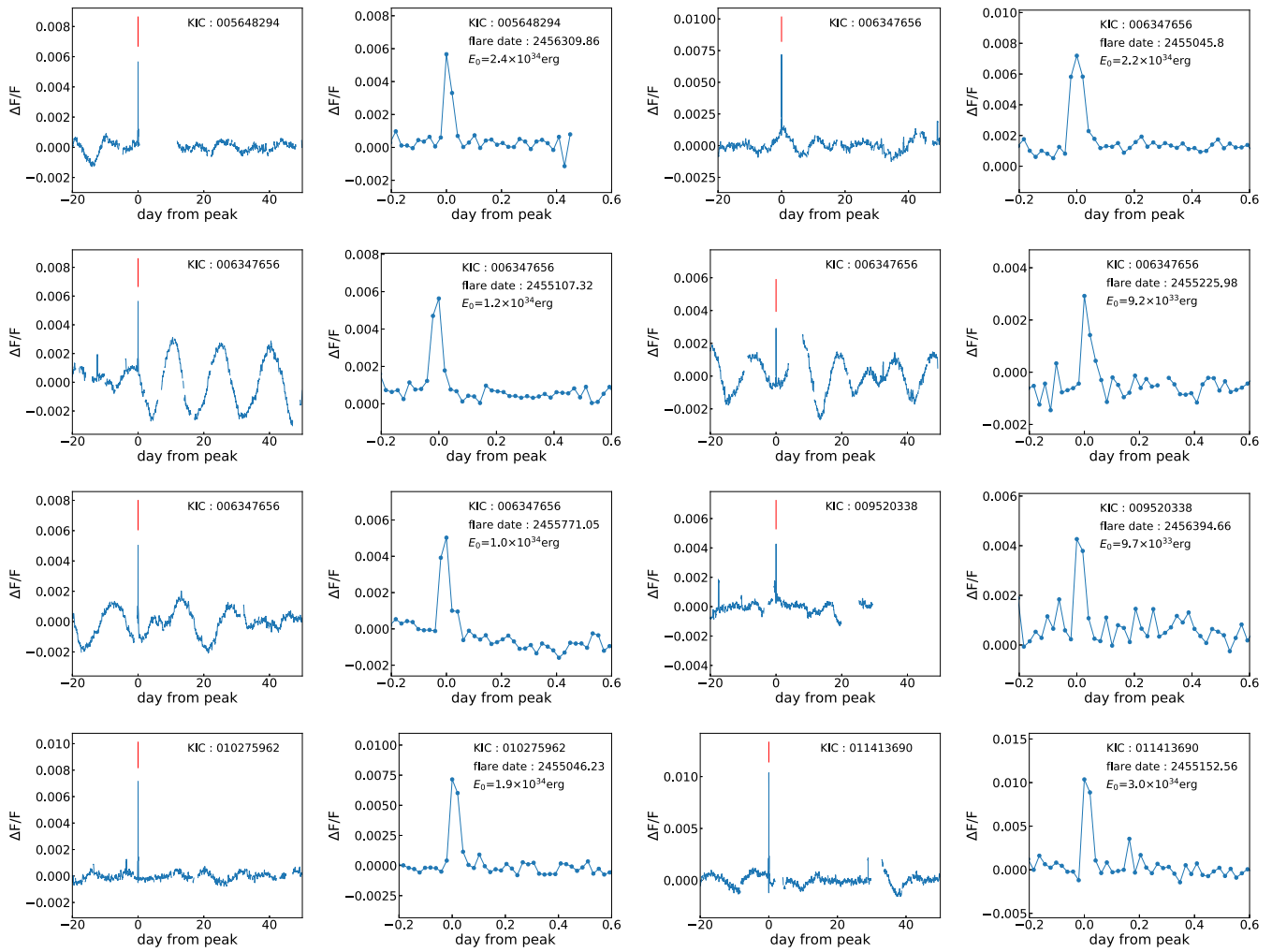
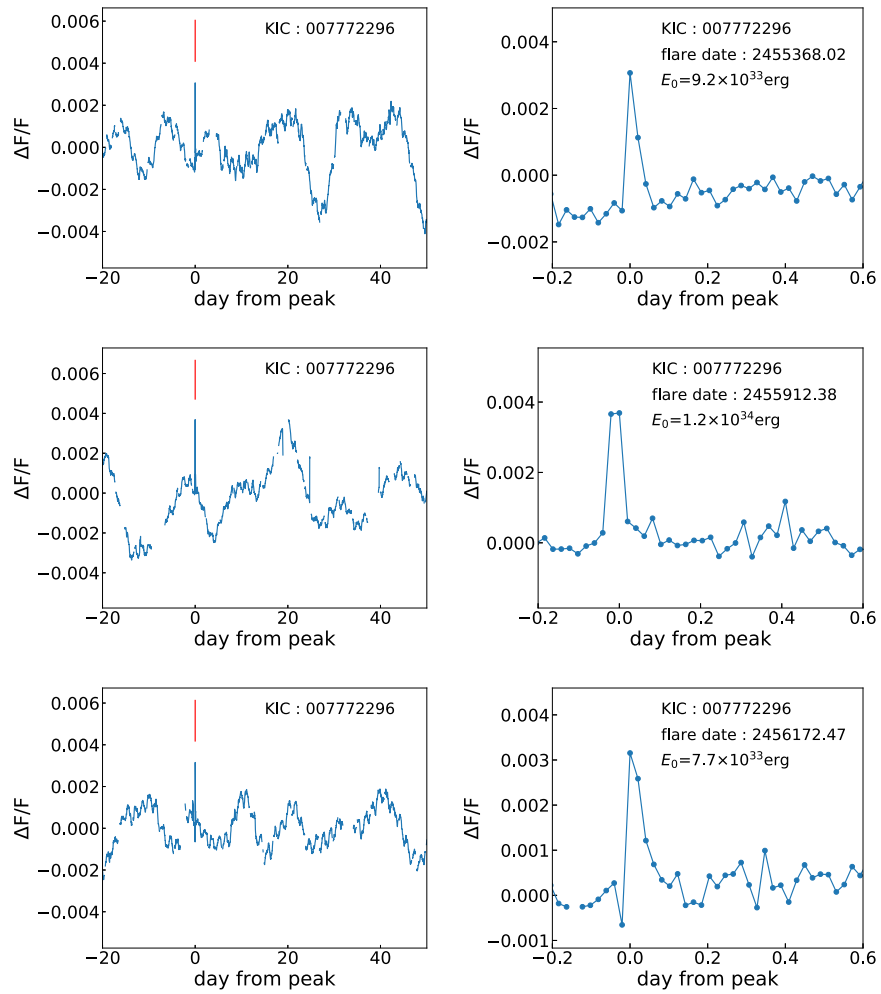**Figure 16.** Same as Figure 15, but for the five stars that have flag 1 in Table 2.

Figure 17. Same as Figure 15, but for the star KIC007772296, which has flag 2 in Table 2.
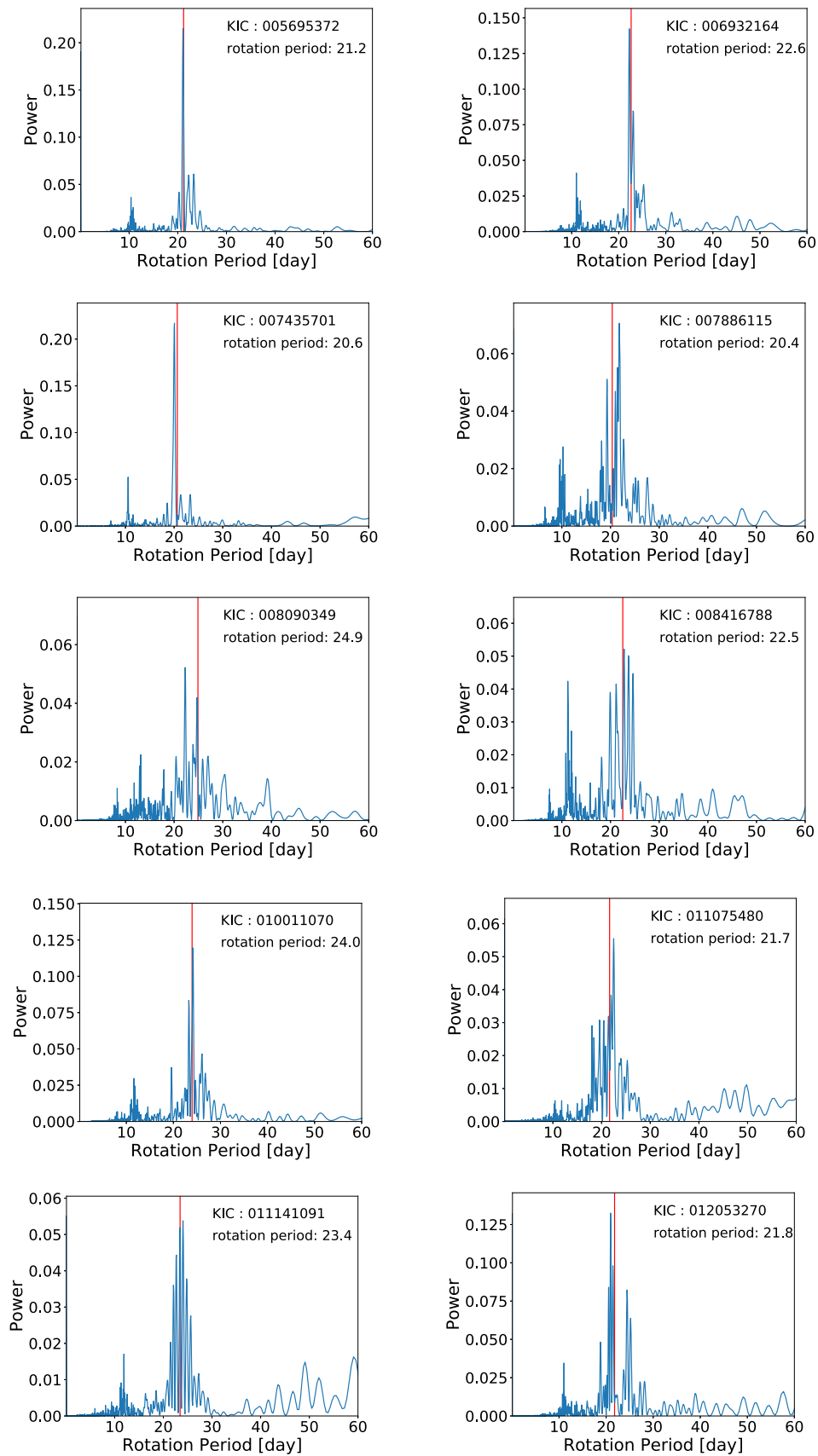
Figure 18. Lomb–Scargle power spectra of the light curves of the 10 Sun-like superflare stars that have no flags in Table 2. The red vertical line in the panels indicates the rotation period $P_{\rm rot}$ values reported in McQuillan et al. (2014). These same $P_{\rm rot}$ values are written with the star IDs (Kepler IDs) in the upper right corner of the panels.
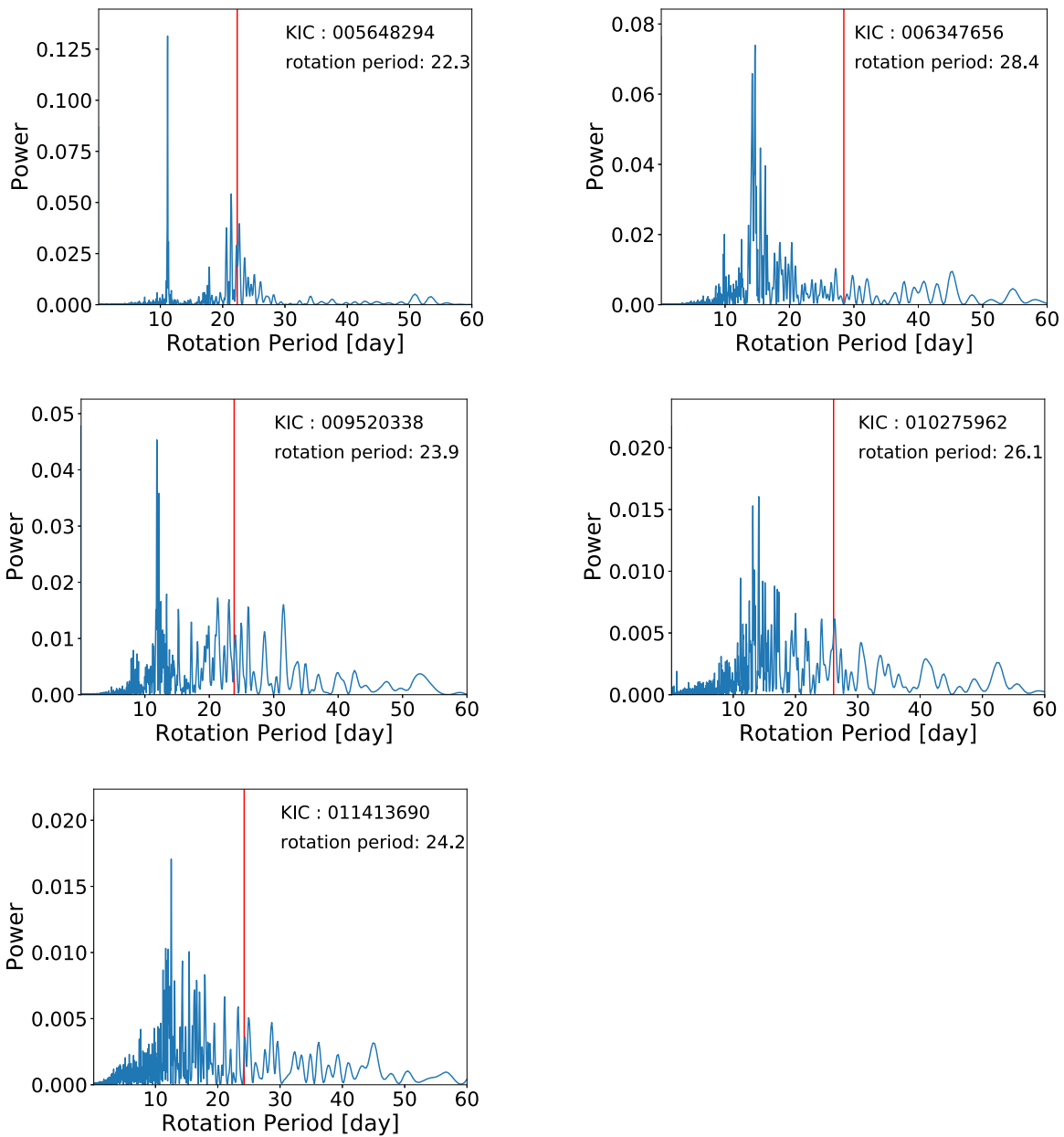
Figure 19. Same as Figure 18, but for the five stars that have flag 1 in Table 2.
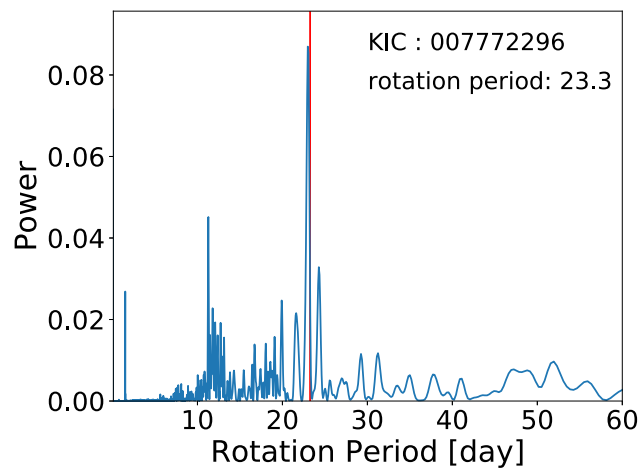

Figure 20. Same as Figure 18, but for the star KIC007772296, which has flag 2 in Table 2.

Table 5
Classification Changes of Two Superflare Stars, KIC 009944137 and KIC009766237, Which Were Originally Reported as Sun-like Superflare Stars
(T_{eff} = 5600–6000 K and P_{rot} > 20 days) in Nogami et al. (2014)

Star	Paper	Classification	Reason for Classification
KIC 009944137	Nogami et al. (2014)	Sun-like star	T_{eff} = 5666 ± 35 K,[a] P_{rot} = 25.3 days, and $v \sin i$ = 1.9 ± 0.3 km s^{-1}[a]
	Notsu et al. (2015a & 2015b)	Not Sun-like star	P_{rot} = 12.6 days by estimating the rotation period using the longer data of Kepler (quarters 2–16: ~1500 days) compared with those in Nogami et al. (2014; quarters 0–6: ~500 days).
	Notsu et al. (2019)	Sun-like star	P_{rot} = 24.4 days by using the rotation period value reported in McQuillan et al. (2014), which estimates rotation periods with the automated autocorrelation-based method
	This study	Sun-like star candidate	Not included in the classification of superflare stars in this study (see Section 3.1), since the amplitude of the rotational brightness variation is so small that the Amp value is not reported in McQuillan et al. (2014), and the accuracy of the P_{rot} value is considered to be low
KIC 009766237	Nogami et al. (2014)	Sun-like star	T_{eff} = 5606 ± 40 K,[a] P_{rot} = 21.8 days, and $v \sin i$ = 2.1 ± 0.3 km s^{-1}[a]
	Notsu et al. (2015a & 2015b)	Not Sun-like star	P_{rot} = 14.2 days by estimating the rotation period using the longer data of Kepler (quarters 2–16: ~1500 days) compared with those in Nogami et al. (2014; quarters 0–6: ~500 days).
	Notsu et al. (2019)	Sun-like star	P_{rot} = 41.5 days by using the rotation period value reported in McQuillan et al. (2014), which estimates rotation periods with the automated autocorrelation-based method
	This study	Sun-like star candidate	Not included in the classification of superflare stars in this study (see Section 3.1), since the amplitude of the rotational brightness variations is so small that the Amp value is not reported in McQuillan et al. (2014), and the accuracy of the P_{rot} value is considered to be low

Note.
[a] The values of effective temperature T_{eff} and projected rotation velocity $v \sin i$ are estimated from our spectroscopic data (Nogami et al. 2014).

Appendix B
Sun-like Superflare Stars with Spectroscopic Observations

As described in Section 1 of this paper, one of the most important purposes of superflare studies is clarifying whether slowly rotating Sun-like stars really have superflares or not. In this study, we have found 15 Sun-like superflare stars from Kepler data as listed in Table 2, but the results from Kepler photometric data only are not enough. Our previous spectroscopic observations of 64 solar-type superflare stars with various rotation periods (Notsu et al. 2013a, 2015a, 2015b; & 2019; Nogami et al. 2014) have suggested that (i) more than half of solar-type superflare stars are single stars and (ii) quasiperiodic brightness variations of the stars can be used for estimations of rotation period and starspot coverage. However, most of the observed stars in our previous spectroscopic observations are stars with P_{rot} < 20 days, and they are not Sun-like stars (T_{eff} = 5600–6000 K and P_{rot} > 20 days). Because of this, we cannot finally conclude whether the above results (i) and (ii) can be fully applied to Sun-like superflare stars with P_{rot} > 20 days. It is important to investigate each Sun-like superflare star with spectroscopic observations and confirm that it is really a Sun-like superflare star.

Among the observed stars in our previous spectroscopic observations, Nogami et al. (2014) reported that two superflare stars (KIC 009944137 and KIC 009766237) were confirmed to be Sun-like stars on the basis of the rotation period values (P_{rot}) from Kepler photometric data and the projected rotation velocities ($v \sin i$) from the spectroscopic data (see Table 5). However, the remark that these two stars are Sun-like superflare stars has changed, as summarized in Table 5. Finally, these two stars are not included in the 15 Sun-like superflare stars in this study (Table 2), since the accuracy of P_{rot} as a result of Kepler photometric observations is considered to be low (see Table 5). Note that the accuracy of $v \sin i$ observations by the high-dispersion spectrograph on board the Subaru 8.2 m telescope

(used in Nogami et al. 2014; Notsu et al. 2015a & 2015b) was good enough to resolve a rotation velocity as slow as the Sun (~2 km s^{-1}).

In Table 2, KIC 006347656 and KIC 010011070 are also included in the Sun-like superflare stars reported in our previous study using Kepler data (Notsu et al. 2019),[15] but they were not observed in our previous spectroscospic observations (Notsu et al. 2013a, 2015a, 2015b; & 2019; Nogami et al. 2014). Since these previous observations were planned in the initial phase of the research on superflares on solar-type stars, we first aimed to investigate the overall properties of all solar-type superflare stars (e.g., whether the brightness variations can be explained by the rotation of stars with large starspots). Therefore, not only slowly rotating Sun-like superflares but also rapidly rotating solar-type superflare stars were important targets of these previous observations. Considering these things, in order to observe as many superflare stars with various rotation periods as possible in the limited allocated time of the Subaru 8.2 m and Apache Point 3.5 m telescopes, we only observed relatively bright superflare stars (Kepler-band magnitude brighter than 14.2 mag) in these previous observations. As a result, since the two superflare stars KIC 006347656 and KIC 010011070 are faint (Kepler-band magnitude fainter than 14.8 mag), they were not included in the target stars of these previous observations.

As a result, the number of Sun-like superflare stars (T_{eff} = 5600–6000 K, P_{rot} ~ 25 days, and t ~ 4.6 Gyr) that have been investigated spectroscopically and confirmed to be "single" Sun-like stars is now zero. Future spectroscopic observations of Sun-like superflare stars are necessary to investigate whether the Sun-like stars really have superflares. Although all 15 Kepler Sun-like superflare stars listed in Table 2 are relatively

---

[15] It is noted that the names of these stars were not explicitly written in Notsu et al. (2019), since we did not show any tables giving the names of stars, but these two stars were included in the data of superflare stars plotted in the figures of Notsu et al. (2019).

faint (all are fainter than 13.5 mag in Kepler-band magnitude, and most of them are fainter than 14.5 mag), it is very important to conduct spectroscopic observations of these 15 Sun-like Kepler superflare stars in order to confirm the validity of the statistical results of superflares on Sun-like stars discussed in this study using Kepler data (e.g., Figure 14).

In addition, nearby bright superflare stars that are found from TESS (Ricker et al. 2015; Tu et al. 2020; Doyle et al. 2020) and will be found from PLATO (Rauer et al. 2014) can also be good targets for future spectroscopic studies.

Appendix C
Superflares on Subgiants

In Section 3.2, we investigated the relationship between the superflare energy (E_{flare}) and the rotation period (P_{rot}) of solar-type superflare stars. From Figure 3, the upper limit of E_{flare} in a given period bin has a continuous decreasing trend with the rotation period. As we also described in Section 3.2, this decreasing trend was not reported in our initial study (Notsu et al. 2013b). Notsu et al. (2013b) suggested that the maximum superflare energy in a given rotation period bin does not have a clear correlation with the rotation period. This is because some fraction (∼40%) of superflare stars used in our initial studies (Maehara et al. 2012; Shibayama et al. 2013; Notsu et al. 2013b) are now found to be subgiants (Notsu et al. 2019), and

this contamination of subgiants could affect the statistics. In order to check this point, we briefly discuss the superflares on subgiants found from Kepler data.

We searched for superflares on subgiants from the Kepler 30 minute (long) time cadence data (Koch et al. 2010) that were taken from 2009 May to 2013 May (quarters 0–17). As listed in Table 6, we selected the 36,784 G-type subgiant stars on the basis of the evolutionary state classifications (MS/subgiants/red giants/cool MS binaries) and effective temperature (T_{eff}) values listed in Berger et al. (2018), as done for solar-type stars in Section 2.1. Among these subgiant stars, 3533 stars having the values of brightness variation amplitude (Amp) and rotation period (P_{rot}) in McQuillan et al. (2014) are finally used for the flare search process. The method of flare detection and energy estimation is the same as that for solar-type stars in Sections 2.1 and 2.2. As a result, we detected 3780 flares on 168 G-type subgiant stars (see Table 6). We should note here that it is possible that among these "subgiant" stars, not only single evolved subgiant stars but also pre-main-sequence or binary stars (e.g., RS CVn–type binary stars) can be included. This is because of the simple classifications in Berger et al. (2018), which only used the absolute brightness of the star from Gaia-DR2 parallaxes.

Figure 21 shows the relationship between the superflare energy (E_{flare}) and the rotation period (P_{rot}) of subgiant superflare stars. Different from the results of solar-type stars in
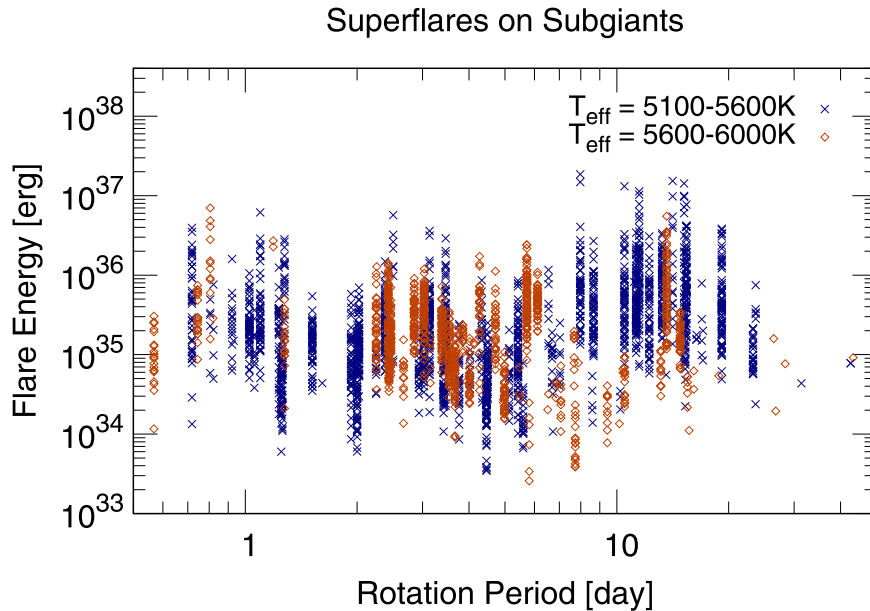

Figure 21. Scatter plot of the superflare energy (E_{flare}) vs. the rotation period (P_{rot}). Basically the same as Figure 3 but for subgiant superflare stars with T_{eff} = 5100–5600 (navy crosses) and 5600–6000 K (dark orange diamonds).

Table 6
The Number of Superflares ($N_{flare,subgiant}$), Subgiant Superflare Stars ($N_{flarestar,subgiant}$), and All Subgiant Stars We Analyzed ($N_{star,subgiant}$)

	$N_{flare,subgiant}$	$N_{flarestar,subgiant}$	$N_{star,subgiant}$
(1) All Kepler stars with T_{eff} and R_{Gaia} values in Baker (2004)			177,911
(2) All subgiants with T_{eff} = 5100–6000 K			36,784
(3) Subgiants with P_{rot} and Amp values in McQuillan et al. (2014)	3780	168	3533
(4) Subgiants with T_{eff} = 5100–5600 K among item (3)	1970	66	820
(5) Subgiants with T_{eff} = 5600–6000 K among item (3)	1135	54	1212

Note. The T_{eff} values and evolutionary state classifications (MS/subgiants/red giants/cool MS binaries) in Berger et al. (2018; see their Figure 5) are used for the classification in this table.
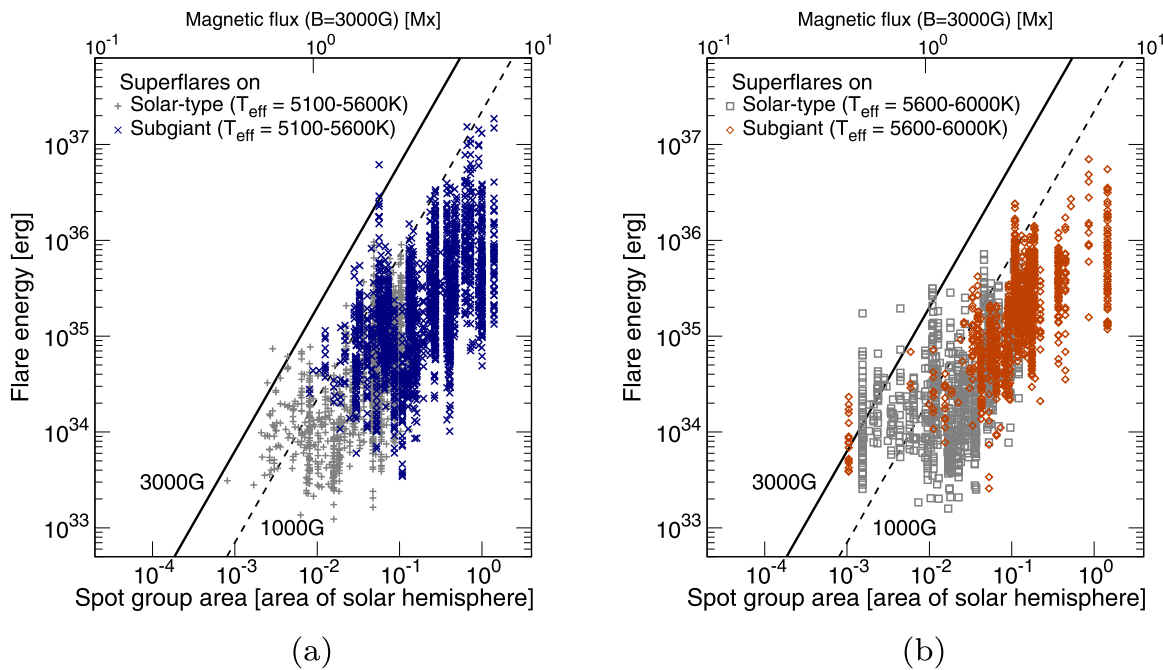
Figure 22. Scatter plot of the superflare energy (E_{flare}) and spot group area (A_{spot}) of superflares on solar-type stars and G-type subgiants. The vertical and horizontal axes, the black solid lines, and the black dashed lines are the same as in Figure 4. (a) Stars with $T_{\mathrm{eff}} = 5100$–5600 K. Gray plus signs are solar-type stars, and navy crosses are subgiants. (b) Stars with $T_{\mathrm{eff}} = 5600$–6000 K. Gray squares are solar-type stars, and dark orange diamonds are subgiants.

Figure 3, the upper limit of E_{flare} values in a given period bin does not show a decreasing trend with the rotation period. Both rapidly rotating ($P_{\mathrm{rot}} \sim 1$ day) and slowly rotating ($P_{\mathrm{rot}} > 10$ days) have superflares up to $\sim 10^{37}$ erg. If some of these subgiants were contaminated with solar-type stars, the decreasing trend of solar-type stars in Figure 3 might be affected. This might be one reason why the decreasing trend was not reported in our initial study (Notsu et al. 2013b).

The upper limit of E_{flare} values of subgiant superflares in Figure 21 is $\sim 10^{37}$ erg, and this is about 10 times larger than the upper limit value of superflares on rapidly rotating solar-type stars in Figure 3. We then discuss this possible difference of the upper limit of E_{flare} values between solar-type and subgiant superflare stars. Figure 22 shows the scatter plot of data of the flare energy (E_{flare}) as a function of the spot group area (A_{spot}) of solar flares and superflare stars. The A_{spot} values of subgiants are estimated from the brightness variation amplitudes by using the same method as used for solar-type stars in Section 3.3. In Figure 22, the data points of subgiant superflare stars tend to be in the upper right side of the panel, compared with those of solar-type superflare stars. This means that superflares on subgiants have larger flare energies and occur on stars having larger starspots. This is consistent with the idea that the flare energy is explained by the magnetic energy stored around large starspots on the stellar surface estimated from Equation (4). As a result, subgiant superflare stars tend to have large starspots and larger energies of superflares compared with solar-type (MS) stars. More detailed discussions of superflares on subgiant stars can be interesting related to dynamo mechanisms on subgiant stars (e.g., Katsova et al. 2018; Kővári et al. 2020), but this is beyond the scope of this paper, and we expect future studies.

ORCID iDs

Yuta Notsu ● https://orcid.org/0000-0002-0412-0849
Hiroyuki Maehara ● https://orcid.org/0000-0003-0332-0811
Kosuke Namekata ● https://orcid.org/0000-0002-1297-9485
Kai Ikuta ● https://orcid.org/0000-0002-5978-057X

References

Airapetian, V. S., Barnes, R., Cohen, O., et al. 2020, IJAsB, 19, 136
Airapetian, V. S., Glocer, A., Gronoff, G., Hébrard, E., & Danchi, W. 2016, NatGe, 9, 452
Allen, J., Frank, L., Sauer, H., & Reiff, P. 1989, EOSTr, 70, 1479
Aschwanden, M. J., Tarbell, T. D., Nightingale, R. W., et al. 2000, ApJ, 535, 1047
Atri, D. 2017, MNRAS, 465, L34
Aulanier, G., Démoulin, P., Schrijver, C. J., et al. 2013, A&A, 549, A66
Ayres, T. R. 1997, JGR, 102, 1641
Baker, D. N. 2004, Introduction to Space Weather, Vol. 656 (Berlin: Springer), 3
Balona, L. A. 2015, MNRAS, 447, 2714
Battersby, S. 2019, PNAS, 116, 23368
Benz, A. O., & Güdel, M. 2010, ARA&A, 48, 241
Berdyugina, S. V. 2005, LRSP, 2, 8
Berger, T. A., Huber, D., Gaidos, E., & van Saders, J. L. 2018, ApJ, 866, 99
Brasseur, C. E., Osten, R. A., & Fleming, S. W. 2019, ApJ, 883, 88
Brown, T. M., Latham, D. W., Everett, M. E., & Esquerdo, G. A. 2011, AJ, 142, 112
Candelaresi, S., Hillier, A., Maehara, H., Brandenburg, A., & Shibata, K. 2014, ApJ, 792, 67
Carrington, R. C. 1859, MNRAS, 20, 13
Cliver, E. W., Hayakawa, H., Love, J. J., & Neidig, D. F. 2020, ApJ, 903, 41
Crosby, N. B., Aschwanden, M. J., & Dennis, B. R. 1993, SoPh, 143, 275
Crosley, M. K., & Osten, R. A. 2018, ApJ, 856, 39
Davenport, J. R. A. 2016, ApJ, 829, 23
Davenport, J. R. A., Hawley, S. L., Hebb, L., et al. 2014, ApJ, 797, 122
Davenport, J. R. A., Mendoza, G. T., & Hawley, S. L. 2020, AJ, 160, 36
Doyle, L., Ramsay, G., & Doyle, J. G. 2020, MNRAS, 494, 3596
Doyle, L., Ramsay, G., Doyle, J. G., Wu, K., & Scullion, E. 2018, MNRAS, 480, 2153
Emslie, A. G., Dennis, B. R., Shih, A. Y., et al. 2012, ApJ, 759, 71
Feinstein, A. D., Montet, B. T., Ansdell, M., et al. 2020, AJ, 160, 219
Gao, Q., Xin, Y., Liu, J.-F., Zhang, X.-B., & Gao, S. 2016, ApJS, 224, 37
Gershberg, R. E. 2005, Solar-type Activity in Main-Sequence Stars (Berlin: Springer)

Giles, H. A. C., Collier Cameron, A., & Haywood, R. D. 2017, MNRAS, 472, 1618

Güdel, M. 2007, LRSP, 4, 3

Günther, M. N., Zhan, Z., Seager, S., et al. 2020, AJ, 159, 60

Hawley, S. L., & Fisher, G. H. 1992, ApJS, 78, 565

Hayakawa, H., Ebihara, Y., Willis, D. M., et al. 2019, SpWea, 17, 1553

Hayakawa, H., Iwahashi, K., Ebihara, Y., et al. 2017a, ApJL, 850, L31

Hayakawa, H., Tamazawa, H., Uchiyama, Y., et al. 2017b, SoPh, 292, 12

Heinzel, P., & Shibata, K. 2018, ApJ, 859, 143

Herbst, K., Grenfell, J. L., Sinnhuber, M., et al. 2019, A&A, 631, A101

Honda, S., Notsu, Y., Namekata, K., et al. 2018, PASJ, 70, 62

Houdebine, E. R., Foing, B. H., Doyle, J. G., & Rodono, M. 1993, A&A, 274, 245

Ikuta, K., Maehara, H., Notsu, Y., et al. 2020, ApJ, 902, 73

Jackman, J. A. G., Wheatley, P. J., Pugh, C. E., et al. 2018, MNRAS, 477, 4655

Karoff, C., Knudsen, M. F., De Cat, P., et al. 2016, NatCo, 7, 11058

Katsova, M. M., Kitchatinov, L. L., Moss, D., Oláh, K., & Sokoloff, D. D. 2018, ARep, 62, 513

Katsova, M. M., & Livshits, M. A. 2015, SoPh, 290, 3663

Kay, C., Airapetian, V. S., Lüftinger, T., & Kochukhov, O. 2019, ApJL, 886, L37

Kővári, Z., Oláh, K., Günther, M. N., et al. 2020, A&A, 641, A83

Koch, D. G., Borucki, W. J., Basri, G., et al. 2010, ApJL, 713, L79

Kowalski, A. F., & Allred, J. C. 2018, ApJ, 852, 61

Kowalski, A. F., Hawley, S. L., Holtzman, J. A., Wisniewski, J. P., & Hilton, E. J. 2010, ApJL, 714, L98

Kurita, M., Kino, M., Iwamuro, F., et al. 2020, PASJ, 72, 48

Leitzinger, M., Odert, P., Greimel, R., et al. 2020, MNRAS, 493, 4570

Lingam, M., & Loeb, A. 2017, ApJ, 848, 41

Linsky, J. 2019, Host Stars and their Effects on Exoplanet Atmospheres, Vol. 955 (Berlin: Springer)

Loomis, E. 1861, AmJS, 32, 318

Lynch, B. J., Airapetian, V. S., DeVore, C. R., et al. 2019, ApJ, 880, 97

Maehara, H., Notsu, Y., Notsu, S., et al. 2017, PASJ, 69, 41

Maehara, H., Shibayama, T., Notsu, S., et al. 2012, Natur, 485, 478

Maehara, H., Shibayama, T., Notsu, Y., et al. 2015, EP&S, 67, 59

Mamajek, E. E., & Hillenbrand, L. A. 2008, ApJ, 687, 1264

Mathur, S., Huber, D., Batalha, N. M., et al. 2017, ApJS, 229, 30

McQuillan, A., Mazeh, T., & Aigrain, S. 2014, ApJS, 211, 24

Mekhaldi, F., Muscheler, R., Adolphi, F., et al. 2015, NatCo, 6, 8611

Metcalfe, T. S., & Egeland, R. 2019, ApJ, 871, 39

Miyake, F., Masuda, K., & Nakamura, T. 2013, NatCo, 4, 1748

Miyake, F., Nagaya, K., Masuda, K., & Nakamura, T. 2012, Natur, 486, 240

Miyake, F., Usoskin, I., & Poluianov, S. 2019, Extreme Solar Particle Storms; The Hostile Sun (Bristol: IOP Publishing)

Mochnacki, S. W., & Zirin, H. 1980, ApJL, 239, L27

Morris, B. M., Curtis, J. L., Douglas, S. T., et al. 2018, AJ, 156, 203

Moschou, S.-P., Drake, J. J., Cohen, O., et al. 2019, ApJ, 877, 105

Namekata, K., Davenport, J. R. A., Morris, B. M., et al. 2020a, ApJ, 891, 103

Namekata, K., Maehara, H., Notsu, Y., et al. 2019, ApJ, 871, 187

Namekata, K., Maehara, H., Sasaki, R., et al. 2020b, PASJ, 72, 68

Namekata, K., Sakaue, T., Watanabe, K., et al. 2017, ApJ, 851, 91

Nizamov, B. A. 2019, MNRAS, 489, 4338

Nogami, D., Notsu, Y., Honda, S., et al. 2014, PASJ, 66, L4

Notsu, S., Honda, S., Notsu, Y., et al. 2013a, PASJ, 65, 112

Notsu, Y., Honda, S., Maehara, H., et al. 2015a, PASJ, 67, 32

Notsu, Y., Honda, S., Maehara, H., et al. 2015b, PASJ, 67, 33

Notsu, Y., Maehara, H., Honda, S., et al. 2019, ApJ, 876, 58

Notsu, Y., Shibayama, T., Maehara, H., et al. 2013b, ApJ, 771, 127

Noyes, R. W., Weiss, N. O., & Vaughan, A. H. 1984, ApJ, 287, 769

O'Hare, P., Mekhaldi, F., Adolphi, F., et al. 2019, PNAS, 116, 5961

Osten, R. A., Kowalski, A., Drake, S. A., et al. 2016, ApJ, 832, 174

Pinsonneault, M. H., An, D., Molenda-Żakowicz, J., et al. 2012, ApJS, 199, 30

Pye, J. P., Rosen, S., Fyfe, D., & Schröder, A. C. 2015, A&A, 581, A28

Rauer, H., Catala, C., Aerts, C., et al. 2014, ExA, 38, 249

Reid, I. N., & Hawley, S. L. 2005, New Light on Dark Stars : Red Dwarfs, Low-mass Stars, Brown Dwarfs (Berlin: Springer)

Reinhold, T., Shapiro, A. I., Solanki, S. K., et al. 2020, Sci, 368, 518

Ricker, G. R., Winn, J. N., Vanderspek, R., et al. 2015, JATIS, 1, 014003

Riley, P., Baker, D., Liu, Y. D., et al. 2018, SSRv, 214, 21

Roettenbacher, R. M., & Vida, K. 2018, ApJ, 868, 3

Rubenstein, E. P., & Schaefer, B. E. 2000, ApJ, 529, 1031

Sammis, I., Tang, F., & Zirin, H. 2000, ApJ, 540, 583

Schaefer, B. E., King, J. R., & Deliyannis, C. P. 2000, ApJ, 529, 1026

Schmieder, B. 2018, JASTP, 180, 46

Schrijver, C. J., Beer, J., Baltensperger, U., et al. 2012, JGRA, 117, A08103

Segura, A., Walkowicz, L. M., Meadows, V., Kasting, J., & Hawley, S. 2010, AsBio, 10, 751

Shibata, K., Isobe, H., Hillier, A., et al. 2013, PASJ, 65, 49

Shibata, K., & Magara, T. 2011, LRSP, 8, 6

Shibata, K., & Yokoyama, T. 2002, ApJ, 577, 422

Shibayama, T., Maehara, H., Notsu, S., et al. 2013, ApJS, 209, 5

Shimizu, T. 1995, PASJ, 47, 251

Soderblom, D. R., Stauffer, J. R., MacGregor, K. B., & Jones, B. F. 1993, ApJ, 409, 624

Takahashi, T., Mizuno, Y., & Shibata, K. 2016, ApJL, 833, L8

Takasao, S., Mitsuishi, I., Shimura, T., et al. 2020, ApJ, 901, 70

Thompson, S. E., Caldwell, D. A., Jenkins, J. M., et al. 2016, Kepler Data Release 25 Notes (KSCI-19065-002) (Moffett Field, CA: NASA Ames Research Center)

Toriumi, S., & Wang, H. 2019, LRSP, 16, 3

Tsurutani, B. T., Gonzalez, W. D., Lakhina, G. S., & Alex, S. 2003, JGRA, 108, 1268

Tu, L., Johnstone, C. P., Güdel, M., & Lammer, H. 2015, A&A, 577, L3

Tu, Z.-L., Yang, M., Zhang, Z. J., & Wang, F. Y. 2020, ApJ, 890, 46

Usoskin, I. G. 2017, LRSP, 14, 3

Valenti, J. A., & Fischer, D. A. 2005, ApJS, 159, 141

Van Cleve, J. E., & Caldwell, D. A. 2016, Kepler Instrument Handbook, Kepler Science Document KSCI-19033-002

Van Doorsselaere, T., Shariati, H., & Debosscher, J. 2017, ApJS, 232, 26

van Saders, J. L., Ceillier, T., Metcalfe, T. S., et al. 2016, Natur, 529, 181

Veronig, A., Temmer, M., Hanslmeier, A., Otruba, W., & Messerotti, M. 2002, A&A, 382, 1070

Vida, K., Leitzinger, M., Kriskovics, L., et al. 2019, A&A, 623, A49

Wright, N. J., Drake, J. J., Mamajek, E. E., & Henry, G. W. 2011, ApJ, 743, 48

Wu, C.-J., Ip, W.-H., & Huang, L.-C. 2015, ApJ, 798, 92

Yamashiki, Y. A., Maehara, H., Airapetian, V., et al. 2019, ApJ, 881, 114

Yang, H., Liu, J., Gao, Q., et al. 2017, ApJ, 849, 36